# Coupled dynamics and evolution of primordial and recycled heterogeneity in Earth's lower mantle

Anna Johanna Pia Gülcher[1], Maxim Dionys Ballmer[2,1], and Paul James Tackley[1]

[1]Institute of Geophysics, Department of Earth Sciences, ETH Zürich, Zürich, Switzerland
[2]Department of Earth Sciences, University College London, London, UK

**Correspondence:** Anna J. P. Gülcher (anna.guelcher@erdw.ethz.ch)

**Abstract.** The nature of compositional heterogeneity in Earth's lower mantle remains a long-standing puzzle that can inform about the long-term thermochemical evolution and dynamics of our planet. Here, we use global-scale 2D models of thermochemical mantle convection to investigate the coupled evolution and mixing of (intrinsically-dense) recycled and (intrinsically-strong) primordial heterogeneity in the mantle. We explore the effects of ancient compositional layering of the mantle, as motivated by magma-ocean solidification studies, and of the physical parameters of primordial material. Depending on these physical parameters, our models predict various regimes of mantle evolution and heterogeneity preservation over 4.5 Gyrs. Over a wide parameter range, primordial and recycled heterogeneity are predicted to co-exist with each other in the lower mantle of Earth-like planets. Primordial material usually survives as mid-to-large scale blobs (or streaks) in the mid-mantle, around 1000-2000 km depth, and this preservation is largely independent on the initial primordial-material volume. In turn, recycled oceanic crust (ROC) persists as large piles at the base of the mantle and as small streaks everywhere else. In models with an additional dense FeO-rich layer initially present at the base of the mantle, the ancient dense material partially survives at the top of ROC piles, causing the piles to be compositionally stratified. Moreover, the addition of such an ancient FeO-rich basal layer significantly aids the preservation of the viscous domains in the mid-mantle. Finally, we find that primordial blobs are commonly directly underlain by thick ROC piles, and aid their longevity and stability. Based on our results, we propose an integrated style of mantle heterogeneity for the Earth, involving the preservation of primordial domains along with recycled piles. This style has important implications for early Earth evolution, and has the potential of reconciling geophysical and geochemical discrepancies on present-day lower mantle heterogeneity.

## 1 Introduction

20  The lower mantle is the largest geochemical reservoir in the Earth's interior, and controls the style of mantle convection and planetary evolution. Despite efficient stirring by vigorous convection over billions of years, the Earth's lower mantle appears to be chemically heterogeneous on various length scales (e.g., Allegre and Turcotte, 1986; van Keken and Ballentine, 1998). Constraining the distribution of this heterogeneity is key for assessing Earth's bulk composition and thermochemical evolution, but remains a scientific challenge that requires cross-disciplinary efforts.

25  On relatively small scales (mm to km), the concept of a "marble cake" mantle has gained wide acceptance, emphasising that much of the mantle is made out of recycled oceanic lithosphere, deformed into narrow streaks of depleted and enriched compositions (Fig. 1a). Partial melting in the upper mantle creates heterogeneity between basaltic (magma) and harzburgitic (residue) end-members, forming a physically and chemically layered oceanic lithosphere. Subsequent injection into the mantle during subduction causes a non-equilibrated mantle that is a mechanical mixture of basalt and harzburgite (Allegre and Turcotte, 1986; Christensen and Hofmann, 1994; Morgan and Morgan, 1999; Xu et al., 2008). Additional small-scale heterogeneity is introduced into the mantle by recycling of continental material through subduction and/or delamination. Such influx of felsic material to the deeper Earth has been used to explain the heterogeneous isotopic compositions of mantle-derived rocks, in particular in terms of trace elements (Hofmann, 1997; Kawai et al., 2009; Stracke, 2012).
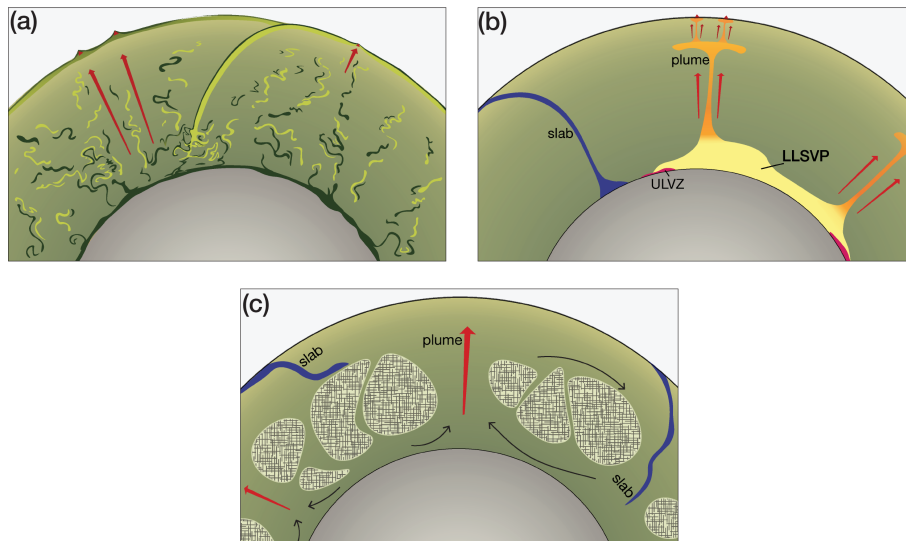


**Figure 1.** Several conceptual models of mantle compositional structure with heterogeneity on various scales. For explanations regarding these heterogeneity styles, the reader is referred to the text. **a) "Marble cake" mantle**, modified after Xu et al. (2008); Woodhead (2015); **b) Thermochemical piles**, modified after Deschamps et al. (2015); **c) Viscous "blobs"**, modified after Becker et al. (1999); Ballmer et al. (2017a).

On larger scales (10s-100s of $km$), compositional heterogeneity may be preserved by delayed mixing of this marble cake with to either intrinsically-dense or intrinsically-strong materials. Intrinsically dense materials may accumulate as piles atop the CMB (Fig. 1b). In particular, the two large low-shear velocity provinces (LLSVPs) in the deep Earth are commonly thought to have resisted mantle mixing due to their thermochemical origin, with an excess density of a few percent compared to pyrolitic material (Hernlund and Houser, 2008). Hypotheses regarding the composition of these dense piles involve recycled oceanic crust (ROC) (e.g., Christensen and Hofmann, 1994; Hirose et al., 2005; Li et al., 2014a), ancient dense material (e.g., Labrosse et al., 2007; Tackley, 2012; Bower et al., 2013; Li et al., 2014b) or a combination of the two (e.g., Tackley, 2012; Ballmer et al., 2016).

On the other hand, intrinsically viscous domains may survive mantle convection and be preserved as "blobs" in the mid-mantle for large timescales (Manga, 1996; Becker et al., 1999; Ballmer et al., 2017a; Gülcher et al., 2020), such as plums in the mantle "plum pudding" (Fig. 1c). The physical properties (e.g., high viscosity) required for long-term preservation of these blobs are thought to be caused by an enrichment in the strong lower-mantle mineral bridgmanite $(Mg,Fe)SiO_3$ (i.e., stabilised by an enrichment in silica). During crystallization of a deep magma ocean at high pressures, $MgSiO_3$ bridgmanite is the relevant liquidus phase over a wide range of conditions and may hence be fractionated, potentially giving rise to such ancient heterogeneity in the mantle (Elkins-Tanton, 2008; Boukaré et al., 2015; Xie et al., 2020). These viscous domains in the mid-mantle may potentially reconcile recent seismic observations of mid-mantle heterogeneity (e.g., Fukao and Obayashi, 2013; Jenkins et al., 2017; Waszek et al., 2018) as well as cosmochemical and geochemical constraints that indicate that the lower mantle hosts an ancient primordial reservoir, potentially enriched in $SiO_2$, with respect to the upper mantle (e.g., Jackson et al., 2010; Mukhopadhyay, 2012). This regime has been successfully reproduced in 2D spherical annulus convection models with composition-dependent rheology (Gülcher et al., 2020). Various styles of primordial heterogeneity preservation were found as a function of its physical parameters, and the survival of sharp-to-diffuse primordial domains in the mid-mantle was proposed for planet Earth (Gülcher et al., 2020). Yet, the employed rheology was simplified and the models did not produce Earth-like tectonic behaviour. Moreover, none of the models explicitly predicted the formation of thermochemical piles in the lowermost mantle, which are perhaps the most evident heterogeneities in Earth's lower mantle (e.g., Solomatov and Stevenson, 1993; Christensen and Hofmann, 1994; Li and Romanowicz, 1996).

Many studies have explored the formation and preservation of either ROC (intrinsically dense) or primordial (intrinsically dense and/or viscous) heterogeneity, but only few if any have quantified mantle dynamics in the presence of different types of heterogeneity with distinct physical properties (e.g., Nakagawa and Tackley, 2014; Li et al., 2014b). Understanding the interplay between recycled and primordial heterogeneity is critical to validate, falsify, and/or integrate the various views on chemical heterogeneity in Earth's mantle (Fig. 1). The goal of the present contribution is to investigate mantle dynamics in the presence of different types of heterogeneity with distinct physical properties (i.e. intrinsically viscous and dense), using Earth-like numerical models of mantle convection. We establish multiple regimes of chemical heterogeneity, dependent on the rheological properties of primordial material. The coexistence of viscous, primordial blobs in the mid-mantle with dense recycled (and possible ancient) piles in the lowermost mantle is robustly predicted in many of our experiments. This coexistence is surprisingly largely independent of the initial compositional layering set-up. Based on these results, we propose that Earth's

mantle is in a hybrid state between "marble cake" and "plum pudding" heterogeneity styles. Finally, the results are put into context with recent discoveries from geochemistry and seismology, and to the long-term evolution of Earth.

## 2   Methods

### 2.1   Numerical technique and initial set-up

In this study, we use the finite-volume code StagYY (Tackley, 2008) to model mantle convection in two-dimensional spherical annulus geometry (Hernlund and Tackley, 2008). The conservation equations for mass, momentum, energy and composition are solved on a staggered grid for a compressible fluid with an infinite Prandtl number. The modelled mantle domain is discretised by $512\times96$ cells. Due to the spherical geometry, as well as vertical grid refinement near the boundary layers and near 660 km depth, the size of grid cells varies between 10 and 35 km in the vertical, and 40 and 80 km in the horizontal direction, respectively. Around 1.2 million tracers (25 tracers per cell) are used to handle non-diffusive advection of composition and temperature. We have performed resolution tests with up to four times the number of grid cells in each direction and up to 50 tracers per cell (see Appendix B). In these tests, we did not observe any significant changes in the overall dynamics of our models. In fact, the preservation of primordial material slightly-to-moderately increases with increasing resolution, as in Gülcher et al. (2020). Thereby, our estimates of primordial-material preservation remain conservative. Boundary conditions are free-slip and isothermal at the top and bottom boundaries, achieved by imposing temperatures of 300 K and 4000 K, respectively. The numerical experiments are purely bottom-heated (no internal heating). Initial temperatures are calculated from an adiabat with a potential temperature of 1900 K, together with the top and bottom boundary layers, and small random perturbations. The resulting temperature profile is $\sim$300 K warmer than that Earth's present-day geotherm. Such high initial mantle temperatures are applied to roughly mimic the thermal evolution of the mantle, with high vigor of mantle convection and near-surface melting that likely occurred in the early Earth (e.g., Davies, 2007; Herzberg et al., 2010).

The initial condition of composition in our models are simplified two-layered (and for selected cases, three-layered) profiles motivated by a fractional-crystallization sequence of the magma ocean (Elkins-Tanton, 2008; Boukaré et al., 2015; Xie et al., 2020). In the lower mantle, bridgmanite is the liquidus phase for a wide range of compositions, while the rest of the mantle evolves towards pyrolitic compositions as bridgmanite is fractionated (Ito and Takahashi, 1989). Similar to previous work (Gülcher et al., 2020), we impose a bridgmanitic "primordial" material layer in the lower mantle with layer thickness $D_{\mathrm{prim}}$ (1568-2230 km, variable between cases). This primordial layer includes 5% pyrolitic "noise", distributed randomly throughout the layer, resulting in an initial primordial layer that is not a pristine fractional-crystallization end-member cumulate. The upper mantle is initially a mechanical mixture of 15% basalt and 85% harzburgite, i.e. close to pyrolitic composition (see Appendix A1). For some models, a third layer is added just above the CMB (150, 200, or 250 km thick), for which we impose the same physical properties as for basalt. This intrinsically dense layer is thought to represent an iron-enriched material, e.g. originating from the last cumulates from a crystallizing basal magma ocean (e.g. Wang et al., 2021) or from ancient crust that settled at the CMB (Elkins-Tanton et al., 2003).

**4**

**Table 1.** Physical properties used in the simulations of this study. UM = upper mantle, LM = lower mantle, PPV = postperovskite. Since we solve for compressible convection, the adiabatic temperature, density, thermal conductivity, thermal expansivity, and heat capacity are pressure-dependent following a third-order Birch-Murnaghan equation of state (Tackley et al., 2013).

| Property | Symbol | Value | Units |
|---|---|---|---|
| Mantle domain thickness | $D$ | 2890 | km |
| Primordial layer thickness* | $D_{prim}$ | 1700-2230 | km |
| Gravitational acceleration | $g$ | 9.81 | m/s$^3$ |
| Surface temperature | $T_s$ | 300 | K |
| CMB temperature | $T_{CMB}$ | 4000 | K |
| Reference viscosity | $\eta_0$ | $5 \cdot 10^{20}$ | Pa·s |
| Lower-mantle viscosity contrast | $\lambda_{LM}$ | 1 | |
| Primordial lower-mantle viscosity contrast* | $\lambda_{prim}$ | 10-500 | |
| PPV viscosity contrast | $\lambda_{ppv}$ | $10^{-3}$ | |
| Primordial buoyancy ratio* | $B$ | 0.07-0.78 | |
| Reference temperature | $T_0$ | 1600 | K |
| Initial reference temperature | $T_{0,ini}$ | 1900 | K |
| Activation energy - UM & LM | $E_a$ | 140 | kJ/mol |
| Activation energy - PPV | $E_{a,PPV}$ | 100 | kJ/mol |
| Activation volume - UM & LM | $V_a$ | $1.8 \cdot 10^{-6}$ | cm$^3$/mol |
| Activation volume - PPV | $V_{a,PPV}$ | $1.4 \cdot 10^{-6}$ | cm$^3$/mol |
| Yield stress | $\tau_{yield}$ | 30 | Mpa |
| Yield stress depth derivative | $\tau'_{yield}$ | 0.01 | MPa/MPa |
| Surface specific heat capacity | $C_{P,0}$ | 1200 | J/(kg·K) |
| Surface thermal conductivity | $k_0$ | 3 | W/(m·K) |
| Surface thermal expansivity | $\alpha_0$ | $3 \cdot 10^{-5}$ | K$^1$ |

## 2.2 Rheology

We apply a visco-plastic rheology, assuming that the material deforms plastically once a critical pressure-dependent yield stress is reached (as in Tackley, 2000; Crameri and Tackley, 2014). Physical and rheological parameters used in this study are listed in Table 1. Viscous deformation is governed by a simplified temperature-, pressure- and composition-dependent Arrhenius-type

105 viscosity law (Newtonian rheology):

$$\eta(T, P, c) = \eta_0 \cdot \lambda_c \cdot exp\left( \frac{E_a + P \cdot V_a}{R \cdot T} - \frac{E_a}{R \cdot T_0} \right) \tag{1}$$

where $\eta_0$ is the reference viscosity at zero pressure and reference temperature $T_0$ (= 1600 K), $E_a$ is the activation energy, $V_a$ is the activation volume, $T$ the absolute temperature, $P$ the pressure and $R$ is the gas constant (8.314 J·mol$^{-1}$K$^{-1}$). As one of the main model ingredients, we consider the composition-dependency of viscosity through prefactor $\lambda_c$ that can be layer

dependent ($\neq 1$ for primordial and post-perovskite compositions, see Table 1 and Section 2.4). In case the grid cell contains a mixture of compositions, the overall cell viscosity is calculated as a mass-weighted geometrical average of the viscosities of different compositions (as in e.g. Tackley and King, 2003).

The effective rheological properties of lower-mantle materials may be well represented by our relatively low effective activation energy and volume (e.g. Yang and Gurnis, 2016). For upper mantle materials, the applied rheological parameters are significantly smaller than lab measurements (Karato and Wu, 1993; Hirth and Kohlstedt, 2003). In our Newtonian rheology formulation, low activation energies can account for the effects of grain-size or stress dependent rheology (e.g., Christensen and Hofmann, 1994; van Hunen et al., 2005; Yang and Gurnis, 2016). Low values of activation volume may result in reduced mechanical decoupling of the lithosphere and asthenosphere in our models, although our choice of yield stress (Table 1) allows for the development of stiff, mobile plates in our models (see below). Also note that the focus of this work is not on modelling the details of upper-mantle dynamics.

We determine models with plate-like behaviour using the same diagnostics as in Tackley 2000, measuring plateness $P$ (the degree to which surface deformation is localized) and mobility $M$ (the extent to which the lithosphere is able to move). For details regarding these diagnostics, the reader is referred to Appendix C. Plate-like behaviour occurs for $P$ close to 1 and $M$ close to or larger than 1 Tackley (2000).

## 2.3 Mantle composition, phase changes and melting

We consider a simplified mantle composition with three lithological components: harzburgite, basalt and primordial material. Accordingly, each tracer carries either a primordial material composition or a mechanical mixture of harzburgite and basalt (hz and bs). The initial composition in the upper mantle is a mechanical mixture of 85% hz and 15% bs, i.e. slightly depleted relative to present-day pyrolitic material (80% hz and 20% bs). Harzburgitic and basaltic materials are treated as a mixture of olivine and pyroxene-garnet systems that undergo different solid-solid phase transitions (for details, see e.g. Nakagawa et al., 2010). Primordial material is not defined in terms of a specific mineral composition, but solely through its material properties. Physical properties and parameters for the phase transitions for each mineral system, and for primordial material, are given in Table 2.

The density profiles of the relevant mantle materials are plotted in Fig. A2. The density profile of primordial material is consistent with that of a bridgmanite-enriched material with a (Mg+Fe)/Si ratio of $\approx 1.0$ (see Appendix A2). We further impose a relatively higher bulk modulus for primordial material than that of the pyrolitic mantle (230 Gpa opposed to 210 GPa), consistent with high-pressure experimental studies of bridgmanite (Wolf et al., 2015). Such higher bulk modulus was found to aid primordial heterogeneity preservation in the mid-mantle (Gülcher et al., 2020). Our reference primordial material roughly corresponds to $Mg_{0.88}Fe_{0.12}SiO_2$ (Tange et al., 2012; Wolf et al., 2015), or any other material with the same density profile (see Appendix A2). The initial chemical density difference between the primordial and pyrolitic layer stabilizes chemical stratification, and its competition with the destabilizing thermal density difference is expressed as the non-dimensional buoyancy

**Table 2.** Phase change parameters used in this study for the olivine, pyroxene-garnet, and primordial system (the latter is parametrised to fit the density profile of a mixture of 40% basalt and 60% harzburgite from Xu et al. 2008). The table shows the depth and temperature at which a phase transition occurs; $\triangle\rho_{\mathrm{pc}}$ and $\gamma$ denote the density jump across the phase transition and the Clapeyron slope, respectively. Phase change parameters used for the olivine and pyroxene-garnet systems are similar to previous studies (e.g., Tackley et al., 2013). Finally, $K_0$ refers to the reference bulk modulus for the system for each individual layer (marked by the depth range), and is increased to 230 GPa for primordial material in the lower mantle (Wolf et al., 2015).

| Depth [km] | Temperature [K] | $\triangle\rho$ [kg/m$^3$] | Phase change width [km] | $\gamma$ [MPa/K] | $K_0$ [GPa]; depth range [km] |
|---|---|---|---|---|---|
| *Olivine ($\rho_{\mathrm{surf}}$=3240 kg/m$^3$)* | | | | | 163; 0-410 |
| 410 | 1600 | 180 | 25 | +2.5 | 85; 410-660 |
| 660 | 1900 | 435 | 25 | -2.5 | 210; 660-2740 |
| 2740 | 2300 | 61.6 | 25 | +10 | 210; 2740-2890 |
| *Pyroxene-garnet ($\rho_{\mathrm{surf}}$=3080 kg/m$^3$)* | | | | | 163; 0-40 |
| 40 | 1000 | 350 | 25 | 0 | 130; 40-300 |
| 300 | 1600 | 100 | 75 | +1.0 | 85; 300-720 |
| 720 | 1900 | 350 | 75 | +1.0 | 210; 720-2740 |
| 2740 | 2300 | 61.6 | 25 | +10 | 210; 2740-2890 |
| *Primordial ($\rho_{\mathrm{surf}}$=3075 kg/m$^3$)* | | | | | 163; 0-40 |
| 40 | 1000 | 260 | 25 | 0 | 145; 40-380 |
| 380 | 1600 | 130 | 75 | 1.675 | 85; 380-660 |
| 660 | 1900 | 450 | 50 | -0.575 | 230; 660-2740 |
| 2740 | 2300 | 61.6 | 25 | 10 | 163; 0-410 |

ratio $B$ (Hansen and Yuen, 1988; Davaille, 1999):

$$B = \frac{\triangle\rho_{\mathrm{C}}}{\triangle\rho_{\mathrm{T}}} = \frac{\triangle\rho_{\mathrm{C}}}{\rho\alpha\triangle T} \tag{2}$$

where $\triangle\rho_{\mathrm{C}}$ and $\triangle\rho_{\mathrm{T}}$ are the relevant compositional and thermal density contrasts; $\rho$ is the density of the lower layer; $\alpha$ is the thermal expansivity, and $\triangle T$ the super-adiabatic temperature contrast between surface and core-mantle boundary (CMB). We calculate $B$ for relevant lower-mantle depths, thus taking depth-dependent parameters $\triangle\rho_{\mathrm{C}}$, $\rho$ (the density of primordial material) and $\alpha$ at 1500 km depth. Accordingly, our reference model with Mg# =0.88 has a buoyancy number of 0.28.

Compositional anomalies carried on tracers evolve from the initial state due to melt-induced differentiation. For example, tracers in the basalt-harzburgite space undergo partial melting as a function of pressure, temperature, and composition to sustain the formation of basaltic crust (for details, see Nakagawa et al. 2010). To approximate melting of primordial material, we assume that any primordial tracer is converted into a tracer with 40% basalt and 60% harzburgite once it crosses the relevant solidus of pyroxenite melting (Pertermann and Hirschmann, 2003) (note that pyroxenes are the low-pressure polymorphs of bridgmanite). We use this 40:60 ratio as it corresponds to a (Mg+Fe)/Si ratio of $\approx$1.0, such as in bridgmanite. This conversion flags the material as "non-primordial", since any melting and related degassing (Gonnermann and Mukhopadhyay, 2007)

155   would likely destroy, or at least dilute, the ancient isotopic fingerprint of the previously "primordial" material. Due to this tracer conversion, the final composition of the non-primordial mantle (from here on termed "ambient mantle") $f_{\text{bs,amb}}^{\text{final}}$ evolves over time as primordial material is processed (melts) in the upper mantle:

$$f_{\text{bs,amb}}^{\text{final}} = \left(f_{\text{bs,amb}}^{\text{ini}} \cdot V_{\text{amb}}^{\text{ini}} + c_{\text{bs,prim}} \cdot V_{\text{prim,molten}}^{\text{final}}\right) / \left(V_{\text{amb}}^{\text{ini}} + V_{\text{prim,molten}}^{\text{final}}\right) \qquad (3)$$

where $f_{\text{bs,amb}}^{\text{ini}}$ is the initial bulk composition of the ambient mantle with volume $V_{\text{amb}}^{\text{ini}}$, $c_{\text{bs,prim}}$ is the conversion factor of primor-
160   dial material into bs-hz space (i.e. 0.4) and $V_{\text{prim,molten}}^{\text{final}}$ is the total volume of primordial material that has melted during model evolution ($= (1 - \chi_{\text{prim}}^{\text{pres}}) \cdot V_{\text{prim}}^{\text{ini}}$ with primordial preservation factor $\chi_{\text{prim}}^{\text{pres}} = \frac{V_{\text{prim}}^{\text{final}}}{V_{\text{prim}}^{\text{ini}}}$).

## 2.4 Parameter study

We systematically investigate the styles of chemical heterogeneity in the mantle as a function of the physical properties of primordial material. The physical properties of the $(\text{Mg,Fe})\text{SiO}_3$-enriched primordial material explored are the intrinsic density
165   (FeO-enrichment in $(\text{Mg,Fe})\text{SiO}_3$) and viscosity contrast (silica enrichment) relative to pyrolite (as in Ballmer et al., 2017a; Gülcher et al., 2020). Accordingly, the density profile of primordial material is shifted throughout the mantle, intrinsically changing the initial buoyancy ratio $B$ between the models (ranging from 0.07 to $\approx$0.57, see eq. (2) and Table **??**). The approximate primordial material Mg# thereby ranges from 0.9-0.86 (see Appendix A2). A viscosity contrast $\lambda_{\text{prim}}$ ($\lambda_{\text{c}}$ in eq. 1 for primordial material) is imposed between primordial material and pyrolitic mantle material in the lower mantle, motivated by
170   the high viscosity of bridgmanite relative to ferropericlase (Yamazaki and Karato, 2001; Girard et al., 2016).

Additionally, we varied the initial conditions of chemical layering in the models (see Appendix A1). We varied the initial layer thickness of primordial material $D_{\text{prim}}$ such that the final composition of the ambient (i.e., convecting) mantle is similar for all models, roughly consisting of a mechanical mixture of 25% ROC and 75% harzburgite. This value ($f_{\text{bs,amb}}^{\text{final}} = 0.25$) is appropriate for the Earth, particularly if considering that the ambient lower mantle may be moderately enriched in ROC
175   compared to the upper mantle in the present-day (e.g., Murakami et al., 2012; Ballmer et al., 2015; Mashino et al., 2020; Yan et al., 2020). As $f_{\text{bs,amb}}^{\text{final}}$ for any given model depends on the extent of primordial-material processing over time, which creates basaltic materials through near-surface melting (eq. 3), $D_{\text{prim}}$ (i.e., initial volume of primordial material) is set to a different value for a given combination of parameters $B$ and $\lambda_{\text{prim}}$. The applied $D_{\text{prim}}$ range from 1569 km to 1844 km (i.e., 60-75 v% of the lower mantle) between the models. These choices for the initial conditions of our models lead to final ambient-mantle bulk
180   compositions of $f_{\text{bs,amb}}^{\text{final}} = 0.24 - 0.26$, i.e., very close to our target value for all cases. In order to calculate these appropriate values for $D_{\text{prim}}$ in the first place, we ran an additional suite of test models with a constant initial volume of primordial material. From the predictions of these test models, the appropriate values for $D_{\text{prim}}$ for each case of the main model suite were computed according to eq. (3). For more details on this approach and the results of the test suite, see Appendix D.

Finally, for selected cases, we include a thin, dense FeO-rich layer just above the CMB (see Section 3.3), and compare model
185   outcomes with those of corresponding models in the main model suite (2-layered).

# 3 Results

We have conducted a total of 119 numerical experiments for this study. The relevant model parameters and selected output variables of each case are summarised in Tables E1 and E2. We first describe the various heterogeneity styles identified in the models (Section 3.1), and their dependence on composition-dependent rheological parameters (Section 3.2). We then discuss how initial compositional layering affects mantle dynamics and chemical heterogeneity preservation (Section 3.3). Finally, we focus on a specific heterogeneity style and analyse the characteristics of the distinct chemical mantle domains, and how they are linked to mantle convection (Section 3.4).

## 3.1 Mantle heterogeneity styles

Our results reveal different styles of long-term convection and mixing in the mantle. We label these regimes in line with previous work on variable styles of primordial heterogeneity preservation (Gülcher et al., 2020) as regimes *I-III*. For all main models, primordial and ROC heterogeneity can coexist in a fully convecting mantle (partial heterogeneity preservation, regime *III*), with several distinct preservation styles (Fig. 2). A subset of the test experiments predicted various styles of stable chemical layering (regime *II*), which are summarised in Section 3.3 and discussed in more detail in Appendix D. In contrast to previous work (Gülcher et al., 2020), we do not observe any models with pervasive convective mixing of ROC as well as primordial mantle materials (regime *I*) in this study.

### 3.1.1 General geodynamic trend

All experiments in the first model suite are characterized by whole-mantle convection and moderate compositional heterogeneity preservation in the lower mantle after 4.5 Gyr of model evolution. Plate-like tectonic behaviour is displayed for most of their evolution (Figs. C1a-e). Their evolution commonly starts as a two-layered convective system that is sustained for several 100s Myr. Almost immediately, weak downwellings develop from the cold thermal boundary layer at the top and are deflected at the compositional interface in the mid-mantle. The onset of convection in the lower layer is delayed with respect to the upper layer. However, progressive heating and cooling of the lower and upper layers, respectively, promotes a whole-mantle overturn at ≈0.2-1 Gyr. During this overturn, much of the primordial material in the lower mantle may reach the upper mantle, and subsequently be processed by extensive near-surface melting. Consequently, basaltic crust is formed that can re-enter the mantle through subduction. Moreover, the strong primordial material is separated into several blobs and/or streaks, that are slowly eroded and entrained by the convecting pyrolitic mantle over billions of years. The final extent of heterogeneity differs between the models; four subregimes are established:

### 3.1.2 Viscous blobs (regime *III.B*)

In many numerical experiments, primordial material is ultimately preserved as blobs in the mid mantle. Here, the primordial material is neutrally buoyant (Fig. A2) and relatively stale. Deformation due to mantle convection is mainly focused along narrow up- and downwelling conduits (Figs. 2a,b), and blobs are variably preserved in poorly-mixed regions in-between.
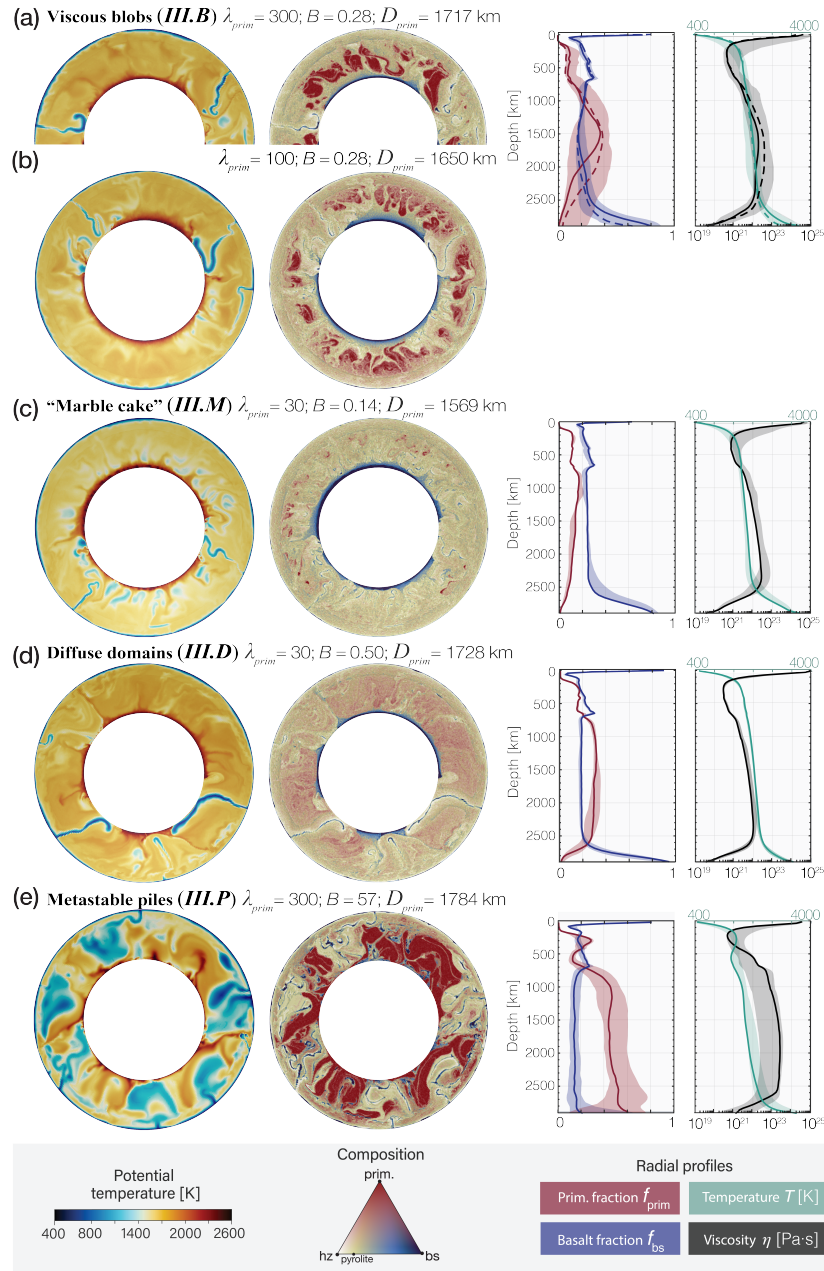
9

**Figure 2.** Left: mantle sections for all sub-styles in regime *III* (partial chemical heterogeneity) at 4.5 Gyr model time; $\lambda_{\mathrm{prim}}$, $B$ and $D_{\mathrm{prim}}$ as labelled. Right: corresponding profiles of primordial fraction, basaltic fraction, temperature and viscosity. These profiles are radially averaged and time-averaged (4.25-4.5 Gyr). The shaded region indicates the range for all models in any given sub-style. Dashed lines refer to the case shown in panel (a).

These blobs periodically rotate and/or are displaced laterally as they are passed by sinking slabs. Occasionally, two blobs coagulate or are separated again, as the convection patterns re-organise through time. When slabs reach the CMB they push away basaltic piles to the side, disconnecting the otherwise continuous basaltic layer at the base of the mantle. The final lower-mantle primordial ($\chi_{\mathrm{prim}}^{\mathrm{LM}}$) and ROC ($\chi_{\mathrm{ROC}}^{\mathrm{LM}}$) heterogeneity range from 8-40 v% and 1.5-6 v%, respectively. This style of material preservation is similar to that described in (Ballmer et al., 2017a; Gülcher et al., 2020), and is here established with the presence of ROC (as piles atop the CMB and "marble cake" streaks throughout the mantle).

### 3.1.3   "Marble cake" mantle (regime *III.M*)

In this style, the final mantle composition is characterized by the preservation of relatively much ROC (4.5-6.5 v%), and little primordial heterogeneity ($< 5$ v%). In addition to large ROC piles in the lowermost mantle, chemical heterogeneity takes the form of thin streaks of recycled and primordial material in an otherwise well-mixed mantle. Ultimately, the mantle is mostly made up of a "marble cake" with both ROC and primordial streaks (Fig. 2c).

### 3.1.4   "Diffuse" primordial domains (regime *III.D*)

Here, primordial heterogeneity is not preserved as coherent blobs or streaks (e.g., with sharp boundaries as in regime *III.B* or *III.M*) but is rather diffusely distributed throughout much of the lower mantle (Fig. 2d). Even though no discrete primordial domains are sustained in the convecting mantle, significant amounts (2-7 v%) of primordial heterogeneity can survive in the lower mantle for 4.5 Gyr model time. As in regime *III.B*, ROC is preserved as piles in the lowermost mantle, as well as streaks throughout the mantle. Aside from these additional structures, regime *III.D* is similar to the diffuse-domain regime detected in Gülcher et al. (2020).

### 3.1.5   Metastable primordial piles (regime *III.P*)

In some numerical experiments, primordial material is preserved as large primordial blobs and streaks that are mostly confined to the lowermost mantle (Fig. 2e). Initial model evolution differs from the main geodynamic trend as hot upwellings form delayed, and even when these upwellings reach the compositional interface, a double-layered convective system is maintained for several 100s of Myr. Gradually, the two-layered system breaks down as subducting slabs break through the lower layer, and in return, hot upwellings, including primordial material, reach upper-mantle depths. Large viscous blobs are confined to, or settle near the CMB due to their relatively large negative buoyancy. Some of the blobs are occasionally pushed up from the CMB by convective currents and intermittently float through the mid-mantle. In contrast to other partial heterogeneity styles, short intervals with low mobility occur in this sub-regime (Fig. C1c). With the addition of the presence of dense ROC heterogeneity (1.5-4 v%) throughout the lower mantle as thin streaks, this regime is similar to previously described as "metastable piles" (regime *III.P*) in Gülcher et al. (2020).
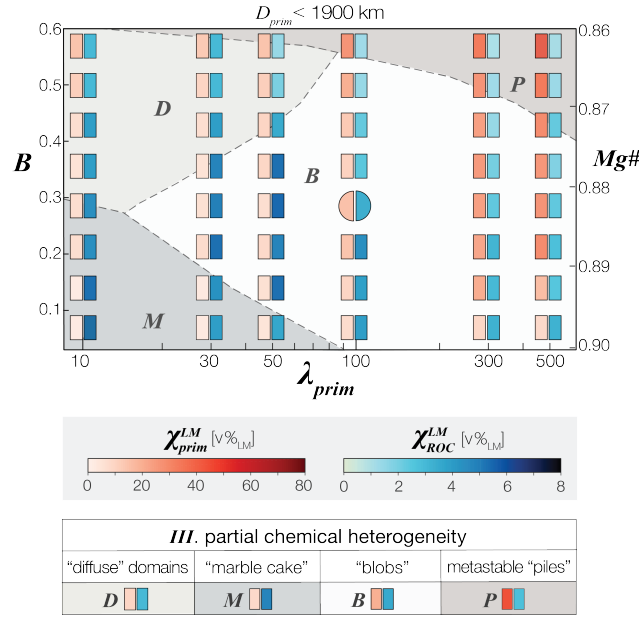
**11**

**Figure 3.** Summary of key results as a function of physical parameters of primordial material for model suite 1 (see text). The vertical axis represents the initial buoyancy ratio $B$, defined at 1500 km depth (Methods and Fig. A2), or the corresponding Mg# of primordial material. The horizontal axis gives the viscosity contrast $\lambda_{\mathrm{prim}}$ between primordial and pyrolitic material in the lower mantle. The fraction of primordial heterogeneity ($\chi_{\mathrm{prim}}^{\mathrm{LM}}$, red) and ROC ($\chi_{\mathrm{ROC}}^{\mathrm{LM}}$, blue) in the lower mantle are averaged between 4.25 and 4.5 Myr model time (for definitions, see Appendix A3). The circle denotes the reference model in this study. Regime boundaries are established based on the style of mantle evolution and chemical heterogeneity: *(III)* partial heterogeneity preservation as marble-cake mantle ("*M*"), marginally stable piles ("*P*"), viscous blobs ("*B*"), or diffuse domains ("*D*").

## 3.2 Influence of physical parameters of primordial material

The regime diagram shown in Figure 3 pinpoints the parameter space where the various heterogeneity styles, discussed above, are identified. The viscous blobs heterogeneity style (*III.B*) occurs for the majority of the parameter space ($\approx \lambda_{\mathrm{prim}} > 20$ and variable $B$), while total volume of the preserved blobs strongly depends on the intrinsic viscosity contrast $\lambda_{\mathrm{prim}}$. High

250 $\lambda_{\mathrm{prim}}$ result in a delayed overturn and more-localised deformation, and hence slow entrainment of primordial material by the convecting mantle (Figs. 3, 2a). In contrast, low $\lambda_{\mathrm{prim}}$ causes an earlier overturn, increases convective vigour and mixing, and prevents large primordial domains to be sustained in the convecting mantle: a "marble cake mantle" (*III.M*) occurs for low $B$; while primordial material is diffusely distributed throughout the mantle (*III.D*) for moderate-to-large $B$. In a narrow parameter space (high $B$ and $\lambda_{\mathrm{prim}}$ of approximately $> 0.45$ and $> 300$, respectively), metastable, primordial "piles" settle due to their

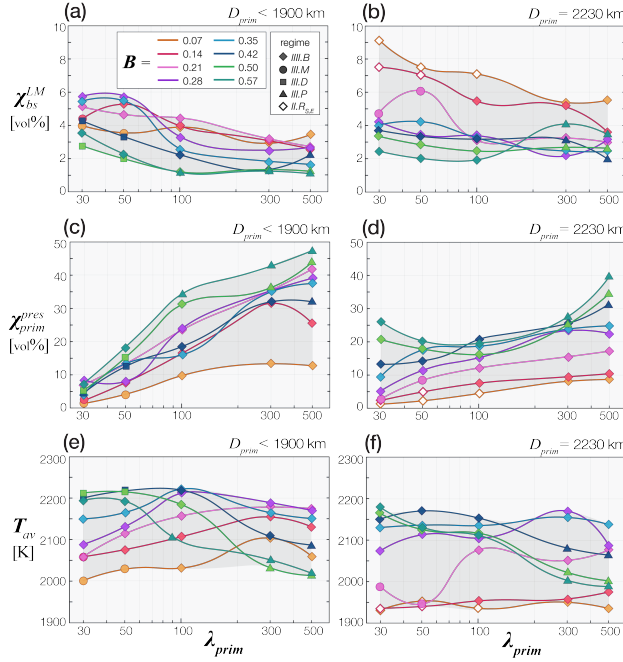255 intrinsic negative buoyancy (regime *III.P*)

**Figure 4.** Output quantities time-averaged between 4.25 and 4.5 Gyr for main model suite (left) and test model suite (right). **a-b)** Primordial preservation factor $\chi_{\text{prim}}^{\text{pres}}$ in v% of initialised primordial material; **c-d)** average mantle temperature; **e-f)** convective vigour. The horizontal axis represents the primordial viscosity contrast $\lambda_{\text{prim}}$, while colours denote different $B$ used in the models.

## 3.3 Influence of initial layering

### 3.3.1 Primordial layer thickness

The model suite discussed above was also run with a fixed primordial layer thickness ($D_{\text{prim}} = 2230$ km, i.e., extending from the CMB up to the top of the lower mantle, as in Gülcher et al., Guelcher2020). The details regarding this model suite are described in Appendix D. As a summary, the final ambient mantle composition greatly varies between the models as highly different amounts of primordial material are processed (as expected from eq. (3)). There is also more variety in geodynamic behavior as two additional sub-styles of stable chemical layering (regime *II*) are identified (see regime diagram in Fig. D2): two-layered convection with an undulating primordial layer preserved for large $B$ (*II.T*), and post-overturn ROC layering for low $B$ and $\lambda_{\text{prim}}$ (*II.R*). Although these regimes are not relevant for present-day Earth, they may be relevant for mantle dynamics within other (exo)planets with slightly different bulk composition, e.g., enhanced in silica. Comparisons of models with equal $B$ and $\lambda_{\text{prim}}$ in both model suites allows us to identify the effect of a different primordial layer thickness on model behavior. Selected model outputs is presented in Fig. 4. Final ROC heterogeneity is increased for most models with more primordial material initialised (Fig. 4a-b), and sub-regime boundaries are slightly shifted as primordial domains are more coherent in comparison with lower $D_{\text{prim}}$ models (Fig. D2). Most notably, the fraction of initialised primordial material that is preserved
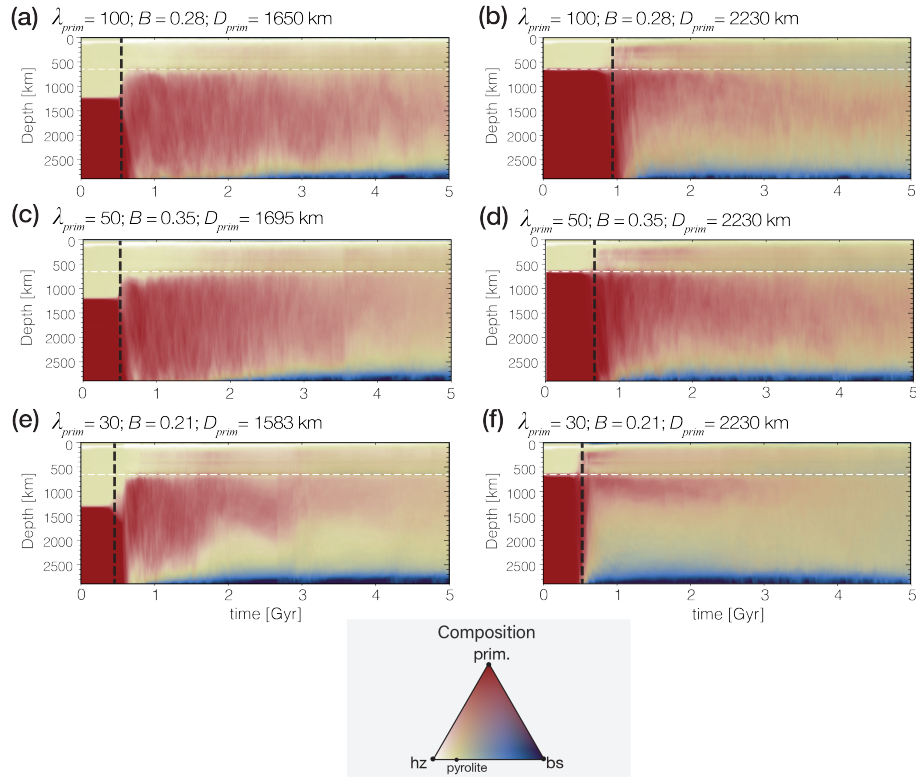
**13**

**Figure 5.** Temporal evolution of the radially-averaged compositional profiles of selected models. Models with variable $D_{prim}$ (main model suite) on the left, and their corresponding model with fixed $D_{prim}$ (= 2230 km, test model suite) on the right for given $B$ and $\lambda_{prim}$: **(a-b)** $B = 0.28$, $\lambda_{prim} = 100$, **(c-d)** $B = 0.35$, $\lambda_{prim} = 50$, **(d-e)** $B = 0.21$, $\lambda_{prim} = 30$. The black dotted line indicates the onset of the compositional overturn. In the test model suite 0, but not in the main suite, significant amounts of primordial material immediately reach the upper mantle after the overturn.

after 4.5 Gyr of mantle stirring ($\chi_{prim}^{pres}$) is similar in both cases or even lower in models with more primordial material initialised (Fig. 4b-c). Moreover, the final internal temperature of all experiments in the test model suite are systematically lower than those the main model suite ($T_{av}$, Fig. 4e-f).

Figure 5 shows the temporal evolution of the radially averaged compositional profiles for selected experiments in both model suites. The compositional overturn (vertical black dashed line in Figure) occurs later for models with a thicker primordial layer, as convective instabilities less rapidly form in the upper, thinner layer to drive the overturn. Moreover, with a primordial-dominated lower mantle, primordial material is immediately swept to upper-mantle depths during the overturn as being displaced by the slabs that sink into the lower mantle (left panels of Fig. 5). Subsequent melting of primordial material and crustal recycling leads to a quick buildup of basaltic piles in the lowermost mantle. In contrast, a thinner primordial layer (left panels of Fig. 5) detaches from the CMB during the overturn and is swept to mid-mantle depths without immediately reaching the upper mantle. At these depths, the primordial material remains relatively stable. Melting of primordial material,
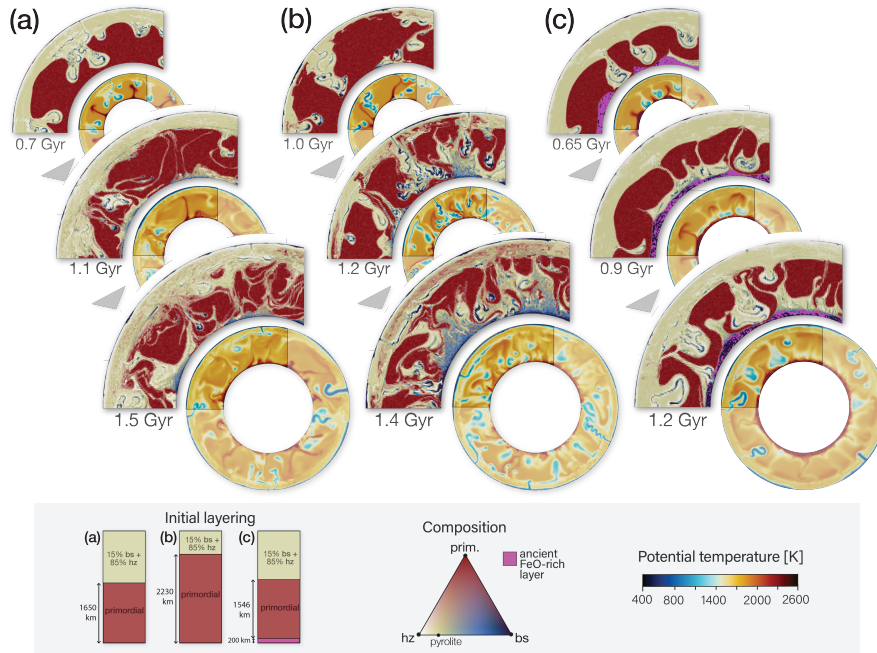
**14**

**Figure 6.** Snapshots during the the compositional overturn phase for three models with equal $B$ (0.28) and $\lambda_{\mathrm{prim}}$ (= 100), but a different initial compositional layering (as shown on the bottom left). The panels provide the potential temperature field, and a zoom-in on the compositional field.

crustal recycling, and ultimately the formation of ROC piles underneath, is thereby delayed. This discrepancy between mantle dynamics and extend of melting affects the subsequent thermal evolution of the models: melting is an efficient mechanism to remove heat from the mantle by transporting heat from the interior to the surface, and enhancing the plates' mobility (Naka-gawa and Tackley, 2012; Lourenço et al., 2016). Thereby, the lower extend of melting in models with a thinner bridgmanitic
285    layer can explain their higher internal temperatures (Fig. 4c). The dynamic behavior described above can also be seen in Figure 6, which shows detailed dynamics of selected models during the compositional overturn.

### 3.3.2    Additional basal FeO-rich layer

We further explore several additional cases that include an additional FeO-rich layer just above the CMB as an initial condition (see Appendix A1). The results of these cases are summarised in Table E1. The imposed material properties of the FeO-rich
290    layer are the same as for basalt (i.e. intrinsically dense, see Fig. A2). Notably, the ancient dense basal layer aids the preservation of bridgmanitic primordial material over time (higher $\chi_{\mathrm{prim}}^{\mathrm{pres}}$). During the compositional overturn, the FeO-rich layer remains at the base of the mantle, while the bridgmanitic material is swept to mid-mantle depths (Fig. 6c). Significant amounts of heat can be retained in this negatively-buoyant layer that acts an insulating boundary layer above the core. Plumes readily form on top of this layer and are less hot than those otherwise directly forming above the CMB, resulting in a less vigorous compositional
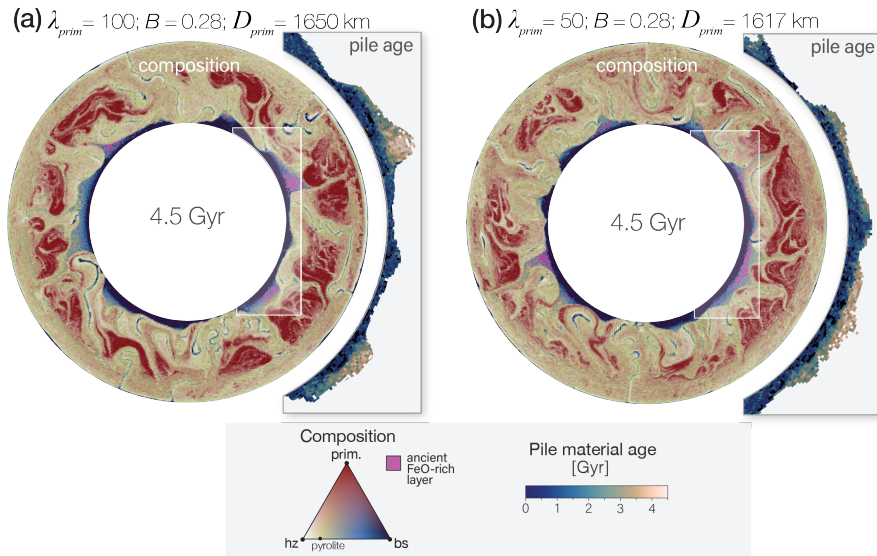
**15**

**Figure 7.** Final snapshots (at 4.5 Gyr) of composition for selected models, $\lambda_{\text{prim}}$ and $B$ as stated in the panels. The models are initialised with a 200 km-thick FeO-rich basal layer (pink), overlain by a **(a)** 1546 and **(b)** 1514 km-thick primordial layer. The panels also show a zoom-in on the formation age of ROC within the piles (defined as $f_{\text{bs}} > 0.6$ and $T_{\text{pot}} > 2000$ K). The formation age quantifies the time since the last melting episode.

overturn and thus an increased coherency of primordial domains. Downgoing slabs separate the initially laterally-connected dense layer into distinct piles, and they also transport ROC to the lowermost mantle, which is then added to the piles of ancient FeO-rich material (see last two panels of Fig. 6c). The incoming ROC material is cooler and thus denser than the hot ancient FeO-rich material. Accordingly, it sinks through the ancient layer to settle directly above the CMB. Over time, much of the ancient FeO-rich material is progressively entrained by mantle upwellings and ultimately processed by near-surface melting. Only a small fraction is preserved after 4.5 Gyr (Table E1), preferably located in the uppermost parts of some thermochemical piles (Fig. 7). The general trend in these piles is aging-upwards: the youngest, most recently subducted (cool) ROC material is at the bottom with progressively older ROC material upwards, and the ancient (hot) FeO-rich material at the very top. Thereby, the piles are thermally stratified, and internal small-scale convection occurs in the lowermost, dense layer. Ultimately, the coexistence of large, coherent bridgmanitic primordial domains with basaltic piles (ROC and ancient) is robustly predicted, even for low $\lambda_{\text{prim}}$ (see Table E1).

### 3.4 Relating dense piles, viscous blobs, and mantle dynamics

Finally, we analysed the potential relationship between dense piles, viscous blobs and mantle dynamics for a model that displays both piles and blobs (model $M_{300\text{dD}}$, regime *III.B*, illustrated in Fig. 2a). Figure 8 shows 2D histograms relating selected model output quantities with one another, including pile characteristics (pile height; formation age of pile material) and mid-mantle characteristics (primordial material fraction, radial velocity, and temperature anomaly over a 1000-2000 km
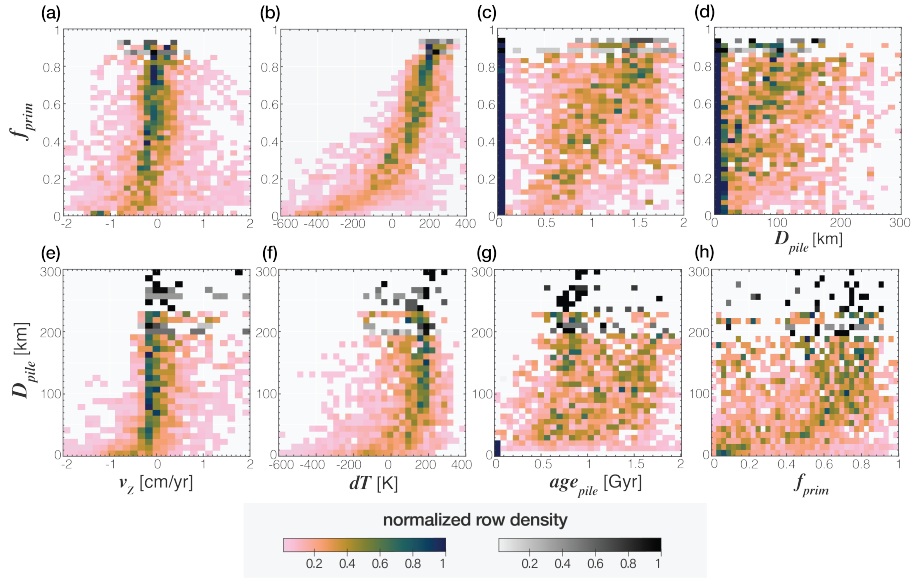
**16**

**Figure 8.** Each panel shows a 2D histogram that relates several selected output quantities of a representative model displaying both primordial blobs and dense piles underneath (regime *III.B*, model $M_{300dD}$, Fig. 2a). For six timesteps (4.25 - 4.5 Gyr with steps of 0.05 Gyr), selected quantities were calculated for each radial column in the model: pile height $D_{pile}$, formation age of pile material $age_{pile}$, mid-mantle primordial material fraction $f_{prim}$, mid-mantle radial velocity $v_z$, and mid-mantle temperature anomaly $dT$. Thermochemical pile thresholds are $f_{bs} > 0.6$ and $T_{pot} > 2000$ K. Mid-mantle is defined are volume-averaged in the dept range of 1000-2000 km. The formation age of pile material is volume-averaged over the full pile thickness and weighted by the basaltic fraction. Each row in the histograms is normalized by the total counts of the row. For rows in grey-scale, the number of counts in these rows represents less than 1% of the total counts.

depth range). Several relations between these parameters can be inferred: first, the presence of primordial material in the mid-mantle is related with little radial dynamics (near-zero $v_z$, Fig. 8a). Similarly, most piles are stable at near-zero radial velocity, although thick ($> 100$ km) piles are also stabilized in regions of upwellings. Second, the absence of primordial domains ($f_{prim} = 0$, bottom rows in Fig. 8e,f) and piles ($D_{pile} = 0$, bottom rows in Fig. 8e,f) is associated with columns of cool downwellings ($v_z < 0$ and $dT < 0$). Third, the presence of much primordial material in the mid-mantle is associated with positive temperature anomalies (Fig. 8b), and thus large primordial blobs (high $f_{prim}$) are typically slightly warmer than average (also see Figs. 2a,b). is also a slight positive correlation between pile height and mid-mantle temperature anomaly: large piles are often related to overlying warm primordial blobs (see below). Although the histograms remain scattered, there is a slight positive trend in formation age of pile material versus mid-mantle primordial fraction, and formation age versus pile height (Figs. 8c,g), indicating that piles containing older material are more often overlain by primordial domains than younger piles, and old ROC tends to be preserved near to top of the piles (see above). Finally, Figures 8d,h indicate a spatial relationship (in radial direction) between the presence of primordial material in the mid-mantle and the height of the underlying ROC material. Even though this relationship is not strict, it indicates that the highest ROC piles tend to be centered just below the largest

primordial blobs. This configuration away from up- and downwellings (Fig. 8b,f) appears to promote the coupled preservation

325 of both these thermochemical domains.

## 4  Discussion

### 4.1  Styles of mantle mixing

Many of the identified dynamic styles of primordial material preservation in our prior study (Gülcher et al., 2020) are here established in the presence of plate-like behaviour and recycling of oceanic crust into the deep mantle. This indicates that

330 primordial material preservation robustly occurs for significant rheological contrasts, regardless of tectonic behaviour or the presence of dense, recycled materials in the lower mantle. This study even shows the robustness of primordial material preservation with respect to initial layering set-up. Despite no detection of models in which both primordial and recycled materials are efficiently mixed throughout the mantle (regime *I* in Gülcher et al. 2020), we expect such a behavior to occur for small rheological contrasts of primordial material in combination with lower density anomalies of ROC than modelled here (Naka-

335 gawa and Tackley, 2014). Indeed, different ROC properties may affect the segregation, accumulation and survival of ROC in the deep mantle (e.g., Christensen and Hofmann, 1994; Hirose et al., 2005; Nakagawa et al., 2010; Mulyukova et al., 2015).

All of our numerical experiments are run in 2D geometry. Admittedly, the planform of mantle flow is different for 3D than for 2D geometry (Ferrachat and Ricard, 1998; Davies, 1990). An additional toroidal component of mantle flow in 3D can enhance mixing relative to mantle flow in 2D with its rather simple geometry of convection. In terms of the preservation of

340 intrinsically-strong heterogeneity, however, we expect competing effects to occur: on one hand, coherent blobs may be difficult to be preserved in the presence of toroidal and poloidal flow components (Ferrachat and Ricard, 1998); on the other hand, mantle flow may be more efficiently guided around viscous blobs in 3D than in 2D geometry (Merveilleux du Vignaux and Fleitout, 2001). Also, sheet-like upwellings in 2D can enhance mixing. Indeed, several studies showed that for high Rayleigh-number convection models, the different geometry of boundary layer instabilities between 2D and 3D does not significantly

345 modify the timescale nor regime of mixing (e.g. Coltice and Schmalzl, 2006; O'Neill and Zhang, 2018), although it is uncertain whether this would be the case in the presence of composition-dependent rheology as modelled here.

The relevance of each regime for terrestrial planet evolution depends on the actual initial compositional profile of the mantle at the onset of long-term solid-state convection. The initial conditions of our models are mainly motivated by an enrichment of a thick, basal layer in $(Mg,Fe)SiO_3$ bridgmanite (and hence in silica with respect to the overlying mantle). This may occur

350 due to fractionation during magma-ocean or basal magma-ocean (BMO) crystallization (e.g., Labrosse et al., 2007). Indeed, bridgmanite is the liquidus phase in a magma ocean over a wide compositional and pressure range (e.g., Ito and Takahashi, 1987; Caracas et al., 2019). Alternatively, incomplete core-mantle equilibration during the last stages of planetary accretion (Deng et al., 2019; Kaminski and Javoy, 2013), or disproportionation of FeO during core formation (Frost and McCammon, 2008; Armstrong et al., 2019), may have promoted the formation of (bridgmanite-enriched) heterogeneity in the lowermost

355 mantle. Moreover, chemical transfer between the outer core and the (basal) magma ocean in a hot early Earth may have caused delivery of $SiO_2$ to the BMO and extraction of iron from the BMO into the core, stabilising bridgmanite as the primary liquidus

phase during prolonged periods of BMO crystallisation (e.g., Trønnes et al., 2019). Indeed, various studies have proposed $SiO_2$-exsolution from the core during secular cooling of the Earth or Earth-like planets (e.g., Badro et al., 2016; Hirose et al., 2017; Helffrich et al., 2018a; Rizo et al., 2019).

## 4.2  A recipe for Earth's lower mantle: "marble cake" plus "plum pudding"

For Earth, geodynamic styles that predict the coupled preservation of primordial material and ROC, such as regimes *III.D* (diffuse primordial domains), *III.M* ("marble cake" mantle), and *III.B* (viscous blobs), can potentially explain a wide range of geophysical, geochemical, and geological constraints. First, these geodynamic styles are consistent with whole-mantle convection operating on Earth, which is motivated by seismic tomographic images of recently ($< 200 \, \mathrm{Myrs}$) subducted lithosphere in the lowermost mantle (e.g., van der Hilst et al., 1997), and deep-rooted plumes that rise through the entire mantle (French and Romanowicz, 2015). Second, they all include the existence of thermochemical piles in the lowermost mantle, which are robustly featured in seismic tomographic studies as two antipodal, anomalously slow domains (LLSVPs) just above the CMB. (e.g., Li and Romanowicz, 1996; Ritsema et al., 1999; Trampert et al., 2004). Third, coupled preservation of primordial and recycled materials in the models agrees with the geochemical record of igneous rocks carrying the footprint of both (old) recycled crust (e.g., Chauvel et al., 1992; Hofmann, 1997; Cabral et al., 2013) and primordial mantle sources, such as $^{182}W/^{184}W$ and $^{142}Nd/^{144}Nd$ isotopic anomalies and/or high $^{3}He/^{4}He$ ratios (e.g., Jackson et al., 2010; Touboul et al., 2012; Rizo et al., 2016; Peters et al., 2018). The specific isotopic fingerprints of the different mantle reservoirs predicted by our models (e.g., primordial and recycled), and the subsequent sampling thereof by mantle plumes, remain key topics for future research. Finally, the plate-like behavior displayed by the numerical models agree with various geological indicators of plate tectonics operating on Earth for at least several $\mathrm{Gyrs}$ before present-day (Korenaga, 2013, and references therein).

Out of the likely geodynamic styles (diffuse domains, "marble cake" mantle, and viscous blobs), the primordial blobs style (*III.B*) is most commonly predicted (Fig. 3). Model predictions for this subregime are also consistent with the stagnation of some slabs in a depth range that is similar to primordial-domain roofs, while other slabs readily sink into the deep mantle (Fukao and Obayashi, 2013), as seen in Figs. 2, 7 and Suppl. Videos (Gülcher, 2021). Furthermore, the presence of viscous domains in the mid-mantle may explain the observation of sharp seismic velocity contrasts in the uppermost lower mantle (850-1100 $\mathrm{km}$ depth), usually occurring away from major upwellings and downwellings (Jenkins et al., 2017; Waszek et al., 2018). Moreover, such bridgmanite-rich regions would suppress the average effects of the pressure-induced spin transition of iron in ferropericlase on seismic properties (Crowhurst et al., 2008; Murakami et al., 2012). Indeed, a recent study noted the absence of the expected signal of this spin transition for pyrolitic compositions at mid-mantle depths in global seismic profiles (Shephard et al., 2020), corroborating the presence of bridgmanite-rich regions in a depth range as predicted here. Finally, in terms of seismic tomography, the lack of clear evidence for primordial domains in the mid-mantle may be related to a trade-off between the seismic effects of their compositional (intrinsically fast bridgmanite, Wentzcovitch et al., 2004) and thermal (slightly warmer than the ambient mantle) anomalies.

Although various alternative hypotheses have been put forward to explain each of the observations above, a hybrid style of present-day Earth mantle heterogeneity as predicted here can provide a unified explanation for these various geochemical and
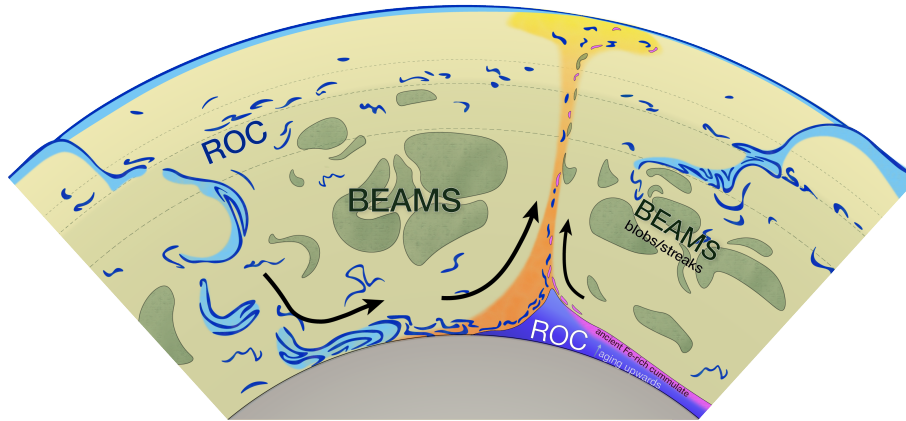
**Figure 9.** sketch of our proposed style of present-day mantle heterogeneity in the Earth. Recycled crustal material (ROC, dark blue) is present throughout the mantle as "marble cake streaks", with enhancement in the mantle transition zone (between 410 and 660 km depth). Moreover, the dense ROC material settles at the CMB to form thermochemical piles. Any ancient basal layer may be preserved within these piles, here proposed on the roof of the piles as predicted by our models (see Figure 8). Finally, primordial $(Mg,Fe)SiO_3$-enriched material is preserved as blobs and streaks that reside in the mid-mantle (dark green) due to its intrinsic strength ("BEAMS": bridgmanite-enriched ancient mantle structures, Ballmer et al., 2017a).

geophysical constraints. This hybrid style is illustrated in Fig. (9) and includes the coexistence of viscous primordial material and dense ROC material in a convecting mantle, with several primordial streaks and/or blobs forming a larger composite bridgmanitic structure (100s-1000 km) around which convective flows is organised. Except for very large $\lambda_{prim}$, this prediction is somewhat different from that in (Ballmer et al., 2017a), who predict large coherent blobs. ROC material is present as "marble-

395    cake" streaks throughout the mantle with local enhancement in the mantle transition zone (MTZ) and at the CMB (i.e., forming thermochemical piles) (as in Nakagawa and Buffett, 2005; Yan et al., 2020). Piles in this regime are mostly of recycled origin, but may include ancient FeO-enriched material that is preserved near their top, if a FeO-rich basal layer ever existed in the early Earth. In this scenario for mantle composition and structure, the upper mantle is on average pyrolitic, while the lower mantle is significantly more enriched in silica, in line with previous studies (e.g., Murakami et al., 2012; Ballmer et al., 2015;

400    Mashino et al., 2020; Yan et al., 2020).

## 4.3    Thermochemical pile layering

Thermochemical piles formed in our models comprise of ROC with varying formation ages. For models including an ancient FeO-rich basal layer, piles consist of both recycled and ancient materials (e.g. a "basal melange", Tackley 2012). Towards the roof of the piles, the formation age of ROC increases, while the overall ROC content decreases (Fig. 7). A radial distinction

405    into regions of a high- and low-ROC content within piles, was also found by Mulyukova et al. (2015). For a high buoyancy ratio of basaltic material, the thermochemical piles consist of a high-density basal-layer covering nearly the entire CMB, overlain by high-topography piles with a much lower fraction of ROC (Mulyukova et al., 2015), as is the case for the thermochemical

piles in our models. Moreover, in our experiments, ancient FeO-rich material survives for several Gyrs at the roof of some piles (Fig. 7). Compositional layering of ancient vs. recycled domains within LLSVPs has been previously proposed (Ballmer et al., 2016; Trønnes et al., 2019), yet with an inverted maturity gradient as found here.

Chemical layering strongly depends on the density profile and rheological properties of the material that makes up the thermochemical piles, which remain poorly constrained. We modelled the ancient FeO-rich basal layer to have the same physical properties as ROC. Final preservation of an ancient basal layer would be advanced, and the maturity gradient potentially inverted, if the layer were enriched in FeO or $SiO_2$ relative to ROC. Such an enrichment may or may not occur depending on the formation scenario of the ancient basal layer, e.g., the style of magma-ocean crystallization (e.g., Labrosse et al., 2007; Ballmer et al., 2017b), or core-mantle interaction (e.g., Hirose et al., 2017; Trønnes et al., 2019). Moreover, ancient crustal rocks may have different chemistry and hence density at lower mantle depths than young basalts (e.g. Herzberg and Rudnick, 2012), which may also affect the layering sequence as seen in our models.

### 4.4 Linking recycled piles, primordial blobs, and mantle dynamics

The slight positive correlation between pile height and overlying primordial material (Fig. 8) differs from the previously conceptional model proposed in Ballmer et al. (2017b), in which the authors suggested that dense mantle material ideally piles up in zones of convergence atop the CMB, free from overlying viscous blobs ("BEAMS"). As we find piles to comprise of older material when overlain by primordial blobs (Fig. 8d,h), we infer that primordial domains can shield piles from any incoming subducted material, and aid their longevity. The presence of primordial domains in the mid-mantle may therefore constrain the shapes and spatial fixity of LLSVP-piles (Torsvik et al., 2010; Dziewonski et al., 2010).

Our results further contribute to the ongoing debate about whether thermochemical piles are intrinsically stable features in the deep mantle which spatially determine mantle convective patterns (Dziewonski et al., 2010; Torsvik et al., 2014), or are rather pushed around by subduction zones (McNamara and Zhong, 2005; Zhang et al., 2010). In our models, piles and blobs both mostly reside well away from lower-mantle downwellings, as they are pushed away from them (Suppl. Videos, Gülcher (2021)). Indeed, as noted in previous studies (e.g., McNamara and Zhong, 2005; Zhang et al., 2010; Schierjott et al., 2020), we observe that downgoing slabs are mainly controlling the spatial distribution of piles (as well as viscous blobs), and not the other way around.

### 4.5 Early-Earth shift in mantle dynamics, tectonics, and chemical sampling

An interesting prediction of our models involves the breakdown of ancient compositional layering ("overturn"), marking the beginning of whole-mantle convection (see Figs. 6, C1.). The timing of the overturn varies between 0.5 and 2.5 Gyr of model evolution, mainly depending on the intrinsic strength of the primordial layer ($\lambda_{prim}$). This overturn triggers a shift in surface-tectonic style, as plate-tectonic behaviour ($P$ and $M$) robustly occurs in the models following the event. For Earth, a major change in geodynamic style is commonly proposed to mark the onset of 'modern-style' plate tectonics (e.g., Bédard, 2018; Condie, 2018, and references therein), shifting from either an (episodic) stagnant lid (e.g., O'Neill et al., 2016; Bédard, 2018; Lenardic, 2018), or a sluggish lid with mostly vertical tectonics (e.g. Rozel et al., 2017; Foley, 2018; Lourenço et al., 2020),

to a mobile-lid style with horizontal "plate-like" tectonics. Estimates for the timing of this event vary between studies (e.g., 2 - 3.2 Ga, Korenaga 2013, and references therein). According to our model predictions, the breakdown of ancient compositional layering may be related to such a tectonic shift in Early Earth. The related stirring of the mantle during the overturn may have drastically changed upper-mantle composition (e.g. Stein and Hofmann, 1994), which is likely followed by the oxygenation of the atmosphere, with implications for the evolution of life (Andrault et al., 2017).

Another implication of this geodynamic shift is that deep-rooted mantle plumes can reach the upper mantle for the first time. Accordingly, the geochemical signatures of mafic rocks of this age should carry stronger lower-mantle signatures compared to older mafic rocks. Many geochemical studies indicate a rapid, widespread change in isotopic signatures in basalts around $\approx$3 Ga (e.g., Gamal El Dien et al., 2020, and references therein). For example, $\mu^{182}W$ anomalies in basalts show a steady trend of mostly positive values for rocks of before $\approx$3 Ga, but display negative values in the modern mantle. This change has previously been attributed to inner-core segregation (Rizo et al., 2019) or the onset of deep slab subduction, recycling of crustal material and sediments (e.g., Liu et al., 2016; Rizo et al., 2019). Here, we propose it may (additionally) be related to the onset of primordial-material entrainment by mantle plumes via whole-mantle convection. The primordial material could have obtained a negative $\mu^{182}W$ signal through $SiO_2$-exsolution from the core (which has a strongly negative $\mu^{182}W$ signature (e.g., Kleine et al., 2009) to the (basal) magma ocean during rapid initial cooling of the planet (e.g., Helffrich et al., 2018b; Trønnes et al., 2019; Rizo et al., 2019).

It must be noted that the modeled thermal evolution of the mantle and related early convective vigor somewhat depends on our parameter choices. Although our models do not take into account heating from radioactive decay or core cooling (Nakagawa et al., 2010), the modelled mantles cool over time with internal potential temperatures from 1900 K to $\sim 1600 - 1650$ K, consistent with petrological constraints for Earth's mantle temperatures over time (Herzberg and Rudnick, 2012). A prior study found that early model dynamics differ as a different initial mantle temperature or core temperature is applied, although the ultimate thermal and chemical structure after 4.5 Gyr does not depend much on these parameters (Nakagawa and Tackley, 2012). In particular, the scale of early mantle flow and the geometry of boundary layer instabilities are different when an evolving core temperature and internal heating sources are incorporated (Nakagawa and Tackley, 2012). With our constant core temperature of 4000 K, early-Earth's CMB heat flow is likely underestimated, and present-day heat flux slightly overestimated. The presence of internal heating from the decay of radioactive nuclides (or heat-producing elements, HPE) increases convective vigour, and decreases the length scales of mantle flow. On the other hand, it suppresses active hot instabilities and mantle plumes, which instead become diffuse and passive return flows (e.g. Mckenzie et al., 1974). Keep in mind that erosion of viscous blobs and the entrainment of primordial material is primarily accommodated by plumes. Nevertheless, considering uniform internal heating is likely to impede preservation, as blobs should heat up and rise into the upper mantle, where they would be efficiently processed. However, HPE are unlikely to be uniformly distributed. In fact, they are unlikely to be incorporated into bridgmanitic material for a wide range of formation scenarios. For example, bridgmanitic magma-ocean cumulates will not incorporate any significant levels of highly-incompatible elements, including HPE (Corgne et al., 2005; Brown et al., 2014). Instead, if most HPE are partitioned into the dense, last MO cumulates (i.e. such as the ancient FeO-rich basal layer discussed in Section 3.3.2), they would be "trapped" in this insulating layer.

## 4.6 Model limitations and outlook

As in any geodynamic study, the numerical models remain a simplified approximation of nature. For example, our model resolution only allows us to simulate relatively large heterogeneities (on scales of several km, or larger). Also, we do not include any felsic material in our models, which may contribute to lower mantle heterogeneity by recycling of continental material (Hofmann, 1997; Stracke, 2012). Furthermore, future investigations are needed to clarify how the heterogeneity styles operate in 3D geometry or in the presence of internal heating sources and core evolution.

The work presented here is primarily a numerical study that establishes various feasible regimes of mantle dynamics and heterogeneity mixing/preservation as a function of initial conditions and primordial-material properties. In the future, a thorough integration with inter-disciplinary constraints on mantle heterogeneity is needed to further establish the applicability of some of our detected regimes for the Earth's (lower) mantle. For example, model results should be quantitatively compared with seismic constraints: piles are predicted to be anomalously hot and dense, which would leave a clear seismic signature (e.g. Wang et al., 2020). On the other hand, bridgmanitic blobs in our models are usually only slightly warmer than typical ambient-mantle temperatures (Fig. 8). Therefore, the related seismic anomalies may be much less evident in tomography, particularly when considering that bridgmanite is slightly faster than ferropericlase (Tsuchiya et al., 2020). Indeed, seismic tomographic images do not show obvious large-scale seismic anomalies in the mid-mantle, and future studies should aim at establishing the presence/absence of these domains in the present-day Earth, for example focussing on seismic anisotropy, or out-of-plane reflections.

## 5 Conclusions

We performed a numerical study to investigate the coexistence of different chemical heterogeneity with distinct physical properties in Earth's lower mantle. Our results demonstrate that:

- Primordial and recycled heterogeneity may coexist in various styles in the mantles of Earth-like planets, depending on their rheological properties (intrinsic density and viscosity).

- The final volume of primordial heterogeneity preserved in the mantle only very weakly depends on the initial thickness of the primordial layer in the range of values explored here (35-65 v% of the total mantle).

- The preservation of coherent viscous blobs in the mid-mantle is enhanced by the existence of an ancient FeO-rich basal layer underneath.

- The coupled existence of viscous, primordial blobs in the mid-mantle with dense, recycled (and partially ancient) piles in the lowermost mantle is a robustly predicted over a wide range of parameters.

- The presence of large viscous blobs in the mid-mantle stabilises the underlying dense thermochemical piles, contributing to their preservation and longevity.

Our results provide a quantitative and dynamic framework for the coupled evolution of recycled and primordial materials in a convecting mantle. For planet Earth, we suggest that the lower mantle may be in a hybrid state between "marble cake" and "plum pudding" style of chemical heterogeneity. Such a hybrid mantle structure may reconcile geochemical evidence for ancient-rock preservation in the convecting mantle through the present-day with seismic evidence for whole-mantle convection.

510 Finally, the breakdown of a stratified system with double-layered convection towards a whole-mantle convective system with plate-tectonic behavior as predicted by our models may be relevant for a major geodynamic "shift" during the Archaean, as is indicated by the geological and geochemical record.

*Code and data availability.* The numerical code is available for collaborative studies by request to P.J. Tackley. The data corresponding to the numerical experiments of this manuscript is too large to be placed online, but they can be requested from the corresponding author.

515 *Video supplement.* Video supplements are available at Zenodo under the identifier https://zenodo.org/record/4767426 (Gülcher, 2021).

## Appendix A: Mantle composition

### A1 Initial layering set-up

The various initial conditions of chemical layering used for this study are illustrated in Figure A1. All of the models include a thick, primordial layer ((Mg,Fe)SiO$_3$-enhanced) in the lower mantle. For cases in the main model suite (panel a), this layer thickness varies between 1564-1844 km, according the results from the test model suite (panel b), in which the primordial layer for all cases and expands from the CMB to the top of the lower mantle (660 km depth). The results of this test suite are presented in Appendix (D3). Finally, selected cases are initialised as a three-layered system (panel c), in which a 200 km-thick FeO-rich layer is imposed just above the CMB, motivated by recent magma ocean crystallization studies that suggest the co-existence of iron-rich bridgmanite with Fe-poor bridgmanite cumulates (Wang et al., 2021). The imposed material properties of the FeO-rich layer are the same as for basalt (i.e. intrinsically dense, see Fig. A2).
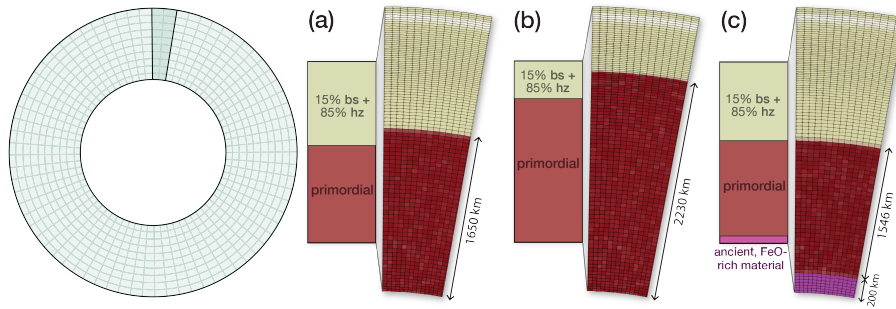


**Figure A1.** Schematic sketch and actual model domain showing the various chemical layering set-ups used for different model suites. The modelled domain is discretised in 512·95 cells, and resolved by over 1.2 million markers. Reference model ($\lambda_{\mathrm{prim}} = 100$; $B = 0.28$) for **a)** Main model suite **b)** Test model suite **c)** 3-Layered set-up. Here, the primordial layer is moved away from the CMB and its thickness $D_{\mathrm{prim}}$ is recalculated to have an equal volume of primordial material initialised as in case (a).

### A2 Density profiles of modelled materials

The density profiles of the relevant mantle materials in this study are plotted in Fig. A2. The profiles of harzburgite and basaltic materials are consistent with those from Xu et al. 2008, whereas that of primordial material is parametrised to be consistent with a rocky material with a (Mg+Fe)/Si ratio of $\approx 1.0$, such as bridgmanite. It resembles that of a solid solution of 40% basalt and 60% harzburgite in Xu et al. 2008 in the upper mantle. Linearly fitting this density profile to those obtained by experimental studies of pure MgSiO$_3$ bridgmanite (Tange et al., 2012) and Mg$_{0.87}$Fe$_{0.13}$SiO$_{0.3}$ bridgmanite (Wolf et al., 2015) materials at mid-mantle depths (1500 km), we estimate that our reference primordial material can be interpreted as corresponding to
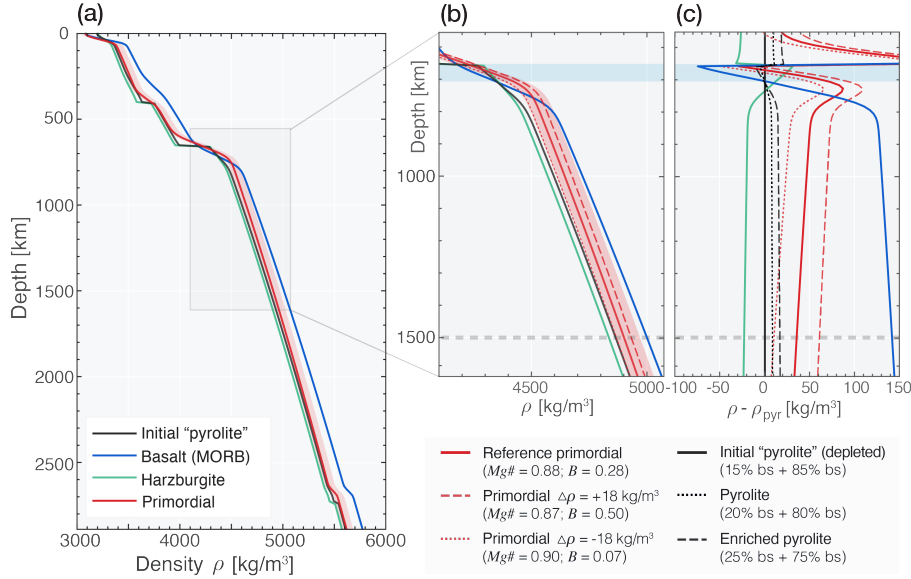
**25**

**Figure A2.** Density profiles for mantle materials used in our simulations. **a)** Density profiles for basalt (light blue), harzburgite (black), initial "pyrolite" (dark blue), and primordial material (red). **b)** Zoom-in on mid-mantle depths. Blue shaded area is the depth range where basaltic material is less dense than pyrolite (transition zone). The grey dotted line is at 1500 km depth, for which the buoyancy number $B$ is calculated (see text). **c)** Relative density contrasts with depth for mantle materials relative to that of the initialized "pyrolitic" material. The red solid line represents our reference primordial material. The dashed and dotted red lines represent primordial material with a buoyancy shift $\delta B = \pm 0.21$. The initial "pyrolite" material is plotted as the black solid line, which is lightly depleted to that of present-day pyrolite (20%bs and 80%hz, black dotted line). A more enriched pyrolite composition (25%bs and 75%hz) is plotted as a black dashed line.

$Mg_{0.88}Fe_{0.12}SiO_2$, or any other material with a similar density profile. To explore the effects of buoyancy ratio $B$, the density

535    profile of primordial material in the main models is shifted throughout the mantle between $-18$ kg/m$^3$ and $+24$ kg/m$^3$ in steps of 6 kg/m$^3$. Thereby, $B$ in the models ranges between 0.07 to 0.57, corresponding to primordial material Mg# ranging from $0.9 \sim 0.86$.

### A3    Visualisation and heterogeneity detection

540    While the composition of an individual tracer is either primordial or a projection on a one-dimensional axis between basalt and harzburgite, that of a grid cell can contain all three possible end-members. The cell composition is therefore visualised with a two-dimensional triangular colour map (Fig. A3a). Two types of lower-mantle chemical heterogeneity are detected in the experiments: primordial ($\chi_{\text{prim}}^{\text{LM}}$) and recycled oceanic crust ($\chi_{\text{ROC}}^{\text{LM}}$). We define $\chi_{\text{prim}}^{\text{LM}}$ and $\chi_{\text{ROC}}^{\text{LM}}$ as the relative volumes of the lower mantle with fractions of primordial material of $f_{\text{prim}} > 0.6$ and of ROC of $f_{\text{bs}} > 0.6$, respectively (Fig. A3b).
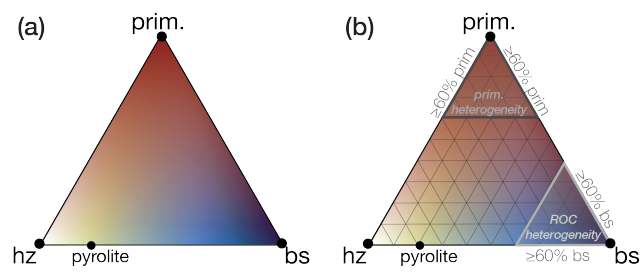
26

**Figure A3. a)** colour scale used in this study to show composition on a grid level, that can consist of harzburgite, basalt and primordial material; **b)** visualisation of the chemical heterogeneity detection. Primordial heterogeneity $\chi_{prim}^{LM}$ is defined as: $f_{prim} > 0.6$; ROC heterogeneity $\chi_{ROC}^{LM}$ is defined as: $f_{bs} > 0.6$.

**Appendix B: Resolution tests**

We performed resolution tests for selected models ($MdD300$, $MdD100$, and $MdD300$) to test the sensitivity of our mantle heterogeneity predictions to grid resolution and tracer density. In these tests, we did not observe any qualitative changes in the overall dynamics of our models or the predicted mantle evolution (or a clear trend in $v_{RMS}$, Fig. B1c). All models with different resolution but the same physical parameters show similar styles of final mantle heterogeneity preservation.

550    For models with a twice higher tracer density than our main suite of models, changes in terms of heterogeneity preservation, $v_{RMS}$, and other proxies of mantle dynamics, are negligible (Fig. B1). These small changes are likely related to a slightly different initial condition that is related to thermal and compositional noise carried at the tracers. For example, the amplitude of the initial compositional noise at the grid level should be effectively smaller for high than for low resolution, as the interpolation from tracers to the grid averages over this random noise.
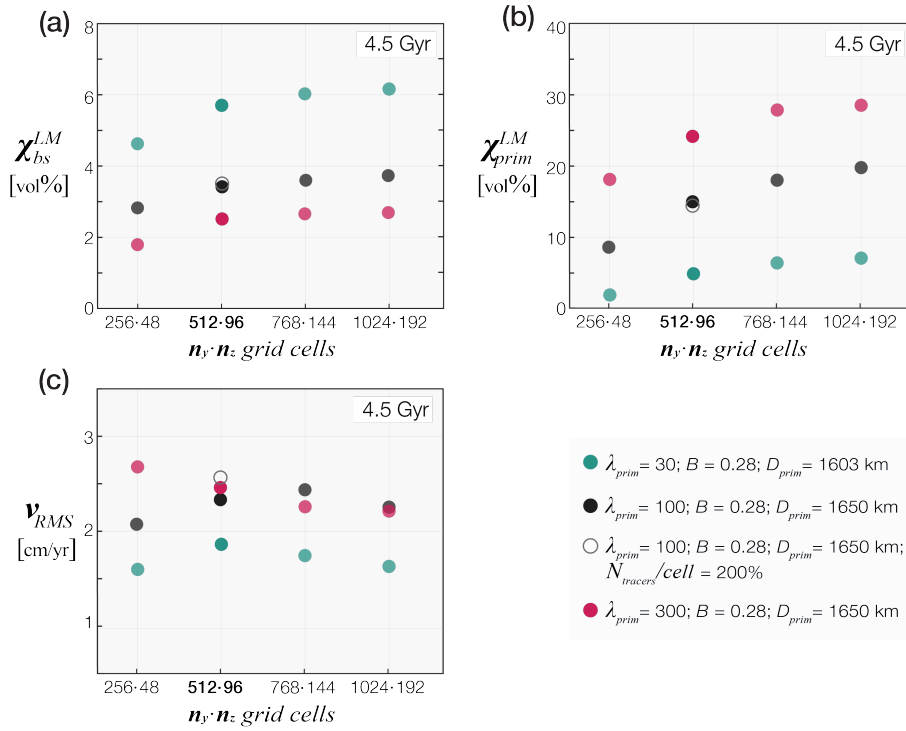


**Figure B1.** Outcomes of our resolution tests based on models $MdD300$, $MdD100$, and $MdD300$ (colour scheme). The horizontal axis of all graphs indicate the different grid resolutions ($n_y \times n_z$) explored. All models presented in the main text and Appendices D-E have a resolution of $512 \times 96$ grid points. The vertical axis differs between panels: the fraction of ROC ($\chi_{ROC}^{LM}$, panel **(a)**) or primordial material ($\chi_{prim}^{LM}$, panel **(b)**) in the lower mantle, averaged over model times 4.25-4.5 Gyr model time. **c)** Root-mean-square velocity of the modelled mantles, averaged over 4.0 and 5.0 Gyr model time.

In contrast, the grid resolution does slightly affect the final quantities of preserved primordial material, and ROC accumulation near the CMB. Small-scale basaltic heterogeneity is better resolved, and thus segregation is slightly more efficient in regions with low viscosity, such as the PPV layer. Also, the boundary between ROC piles and the ambient mantle is better resolved for higher resolution, leading to less artificial entrainment (e.g. Sobouti et al., 2001; Zhong and Hager, 2003). Overall, $\chi_{\mathrm{bs}}^{\mathrm{LM}}$ slightly increases with increasing resolution (Fig. B1a). The preservation of primordial material increases somewhat more substantially with increasing grid resolution: for the three cases explored, $\chi_{\mathrm{prim}}^{\mathrm{LM}}$ increases by ∼20% from cases with a resolution of $512 \times 96$ to high-resolution cases with $1024 \times 192$ (Fig. B1b).

These results suggest that basalt segregation and primordial material preservation is slightly underestimated in our model suite with a resolution of $512 \times 96$, mostly because entrainment is overestimated at lower resolution (as found in e.g. Tackley and King, 2003; Tackley, 2011). Indeed, prior studies have demonstrated the requirement of sufficiently high numerical resolution to better quantify entrainment of intrinsically dense materials by mantle plumes (van Keken et al., 1997; Zhong and Hager, 2003). Along these lines, it is not surprising that entrainment is resolution-dependent, but we have to make a practical choice here to limit computational costs, and allow the exploration of a vast parameter space. Overall, this resolutions test demonstrates that our estimates of heterogeneity preservation, especially in terms of of primordial material, remain conservative.

**Appendix C: Plate-like behavior in numerical models**

As in Tackley (2000), we measure plateness $P$ (the degree to which surface deformation is localized) and mobility $M$ (the extend to which the lithosphere is able to move). Plateness is defined as:

$$P = 1 - f_{80}/f_{80,\mathrm{iso}} \tag{C1}$$

were $f_{80}$ corresponds to the proportion of the surface that localises 80% of the total deformation and the value of $f_{80,\mathrm{iso}}$ for an isoviscous model (about 0.6 for models with Rayleigh number $> 10^6$, Tackley, 2000). The mobility $M$ is the ratio of the root mean-square (RMS) surface velocity to RMS velocity in the whole domain. Plate-like behaviour occurs when $P$ is close to 1 and $M$ is close to or larger than 1 (Tackley, 2000). In Figure C1, the temporal evolution of plateness $P$ and mobility $M$ is plotted for a representative model for each identified mantle heterogeneity style. The models correspond to those presented in Figures 2 and D1. Many of the "partial heterogeneity preservation" models (regime *III*) display plate tectonic behaviour after the onset of whole-mantle convection (i.e., after the compositional overturn).
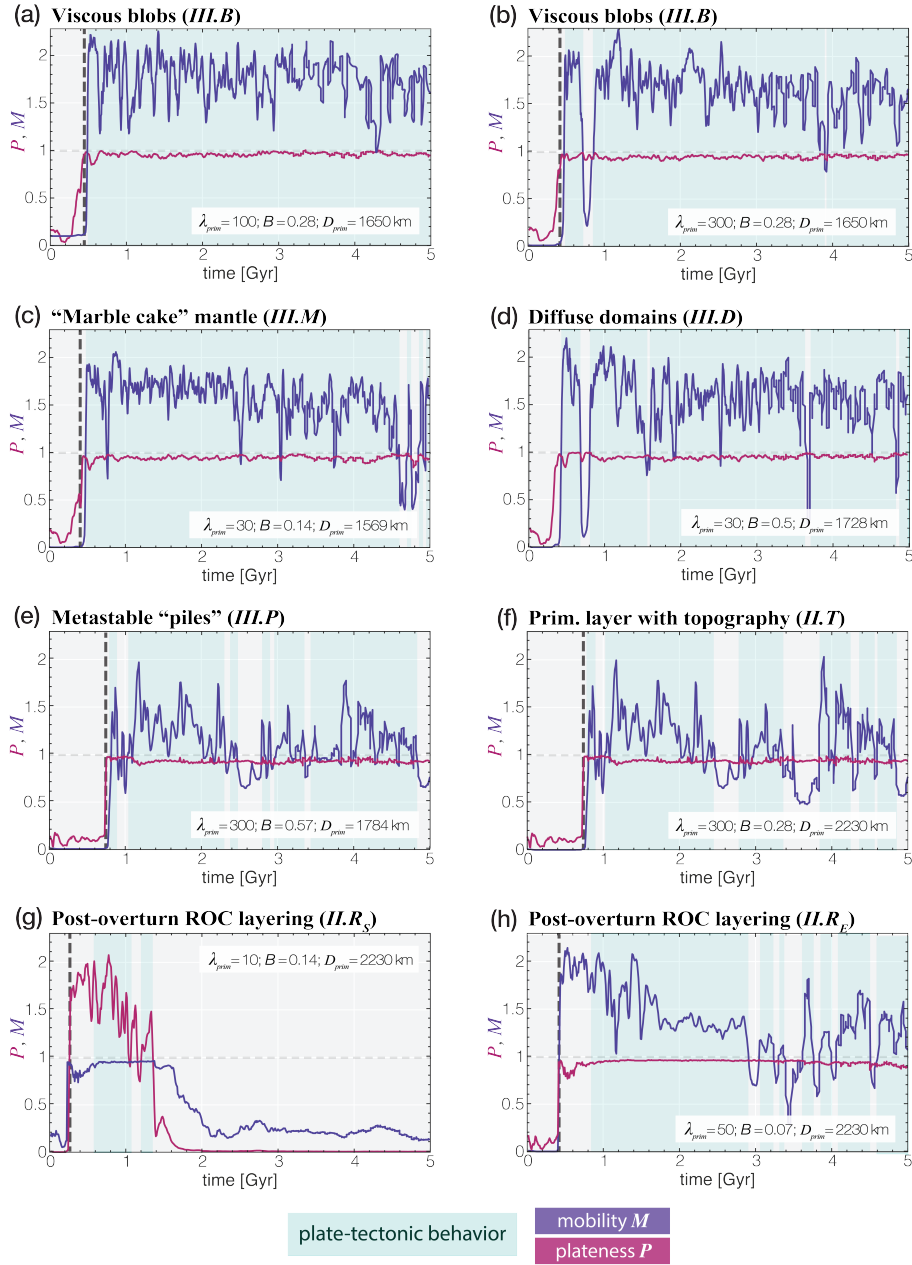
**Figure C1.** Plateness $P$ and mobility $M$ through time for the selected cases of each geodynamic regime identified the models. The black dotted line indicates the onset of the compositional overturn. Plate-tectonic behavior (in line with Tackley, 2000) intervals are marked in shaded blue.

## Appendix D: Additional numerical models (test model suite)

A test model suite was run in a parameter space of $\lambda_{\mathrm{prim}} = [10, 500]$ and $B = [0.07, 0.78]$ with a fixed primordial layer thickness of 2230 $\mathrm{km}$, to solely investigate the style of heterogeneity preservation dependent on $B$ and $\lambda_{\mathrm{prim}}$. The results were then used as an input for the main set of models (see Section D3). In this test model suite, a wide range of chemical heterogeneity preservation styles was observed, as is summarized in Fig. D2a. Many of these include the regimes described in the main text, with the addition of two styles of chemical layering" regime (*II*):

### D1  Description of chemical layering regime (II)

Models within regime *II* display strong compositional layering of the mantle after 4.5 $\mathrm{Gyr}$ of model evolution. These models span a wide range of compositional structures as well as tectonic styles across two subregimes (see Fig. D2b):

### D1.1  Primordial layer with topography *(II.T)*

For large $B$ ($> 0.7$), the initial layered configuration is preserved throughout model evolution. Both mantle down- and up-wellings developing from the thermal boundary layers at the base of the lithosphere and the CMB, respectively, are deflected at the compositional interface. Subsequently, persistent double-layered convection develops with variable topography sustained at the interface as supported by flow in both layers. While primordial material largely remains confined to the lowermost mantle, thin tendrils of ROC are entrained into the lower layer and reach the lowermost mantle (Fig. D1a). Ultimately, primordial heterogeneity occupies about 60 $\mathrm{v\%}$ of the lower mantle, in contrast to a mere 0.2 $\mathrm{v\%}$ of ROC heterogeneity. The tectonic style is characterized by dominant mobile-lid behaviour ($M > 1$) with short intervals of low mobility ($M < 1$, Fig. C1). This regime is similar to that described in Kellogg et al. (1999) and in Gülcher et al. (2020).

### D1.2  Post-overturn ROC layering *(II.$R_S$ and II.$R_E$)*

For near-zero $B$ and $\lambda_{\mathrm{prim}} \leq 100$, models display (semi-)stable chemical stratification of the mantle with a stagnant-lid (*II.$R_S$*) to mobile-lid (*II.$R_E$*) tectonic style. In contrast to the previously described subregime, the chemical layering is formed after a large-scale overturn and is characterized by a thick layer of ROC at the base of the mantle ($>7$ $\mathrm{v\%}$). Initially, double-layered convection is sustained for several 100s $\mathrm{Myr}$ as both weak lower-mantle upwellings and upper-mantle downwellings are deflected at the compositional interface in the mid mantle. However, progressive heating and cooling of the lower and upper mantles, respectively, promotes a whole-mantle overturn at $\sim 0.9$ $\mathrm{Gyr}$. This thick ROC layer forms because much of the primordial material reaches the upper mantle during the overturn, and is subsequently processed by extensive near-surface melting. Consequently, a large volume of basaltic crust forms that soon sinks to the lower mantle. The intrinsic high density of this ROC (Fig. A2a) precludes any further entrainment by upwelling plumes. A small amount of primordial material ($<4$ $\mathrm{v\%}$) is preserved in the uppermost lower mantle, either as a thin diffuse primordial-material enhanced region (regime *II.$R_S$*, $\lambda_{\mathrm{prim}} = 10$, Fig. D1b) or small coherent blobs (regime *II.$R_E$*, $\lambda_{\mathrm{prim}} \geq 30$, Fig. D1c). Subsequent model evolution is characterized by chemical stratification with a ROC layer that mostly fully covers the CMB and small-scale convection within this layer, as

**31**
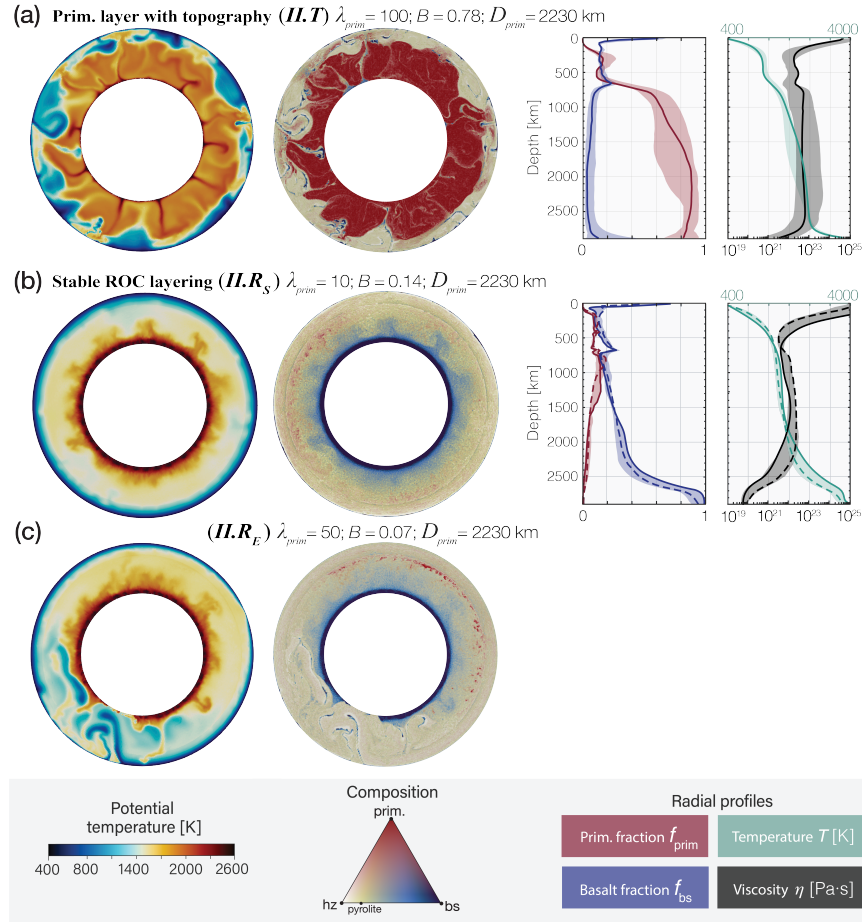
**Figure D1.** Left: Mantle sections of potential temperature (left) and composition (centre) for the two styles within regime *II* (chemical layering) at 4.5 Gyr model time. $\lambda_{\mathrm{prim}}$ and $B$ as labelled. (right) corresponding profiles of primordial fraction, basaltic fraction, temperature and viscosity. These profiles are radially averaged and time-averaged (4.25-4.5 Gyr). The shaded region indicates the range for all models in any given subregime. Dashed lines refer to the case shown in panel (c).

it is heated from below. The upper mantle is strongly depleted (harzburgitic), preventing any significant further melting. In this stratified mantle, convective vigour remains low. The radially averaged temperature and viscosity profiles (Figs. D1b,c) highlight the layering of the mantle, e.g., by showing an intermediate thermal boundary layer. For $\lambda_{\mathrm{prim}} \geq 30$ (regime *II.R$_E$*), plates sporadically sink into the lower-mantle, as mobility $M$ fluctuates over time (Fig. C1c). For $\lambda_{\mathrm{prim}} \leq 10$ (regime *II.R$_S$*), the tectonic style is characterized by a stagnant lid (low $P$ and $M$, Fig. C1b).
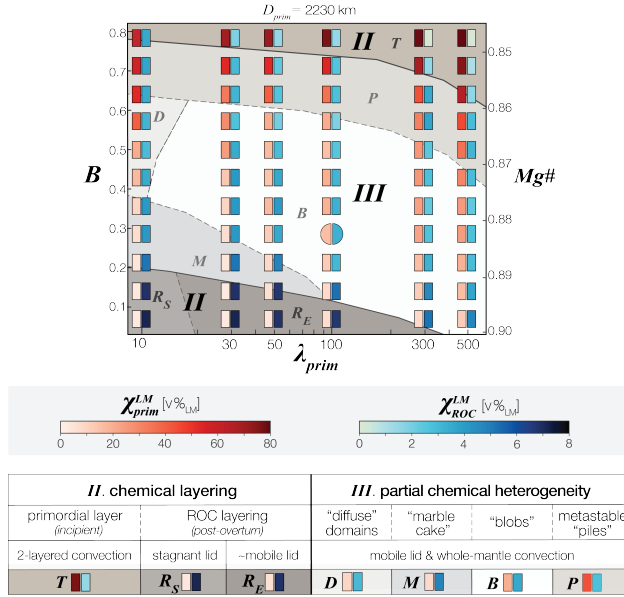
**Figure D2.** Summary of key results as a function of physical parameters of primordial material for the test model suite, in which the initialised primordial layer thickness is constant across the models ($D_{\text{prim}} = 2230$ km). For graph and legend description, see caption of Fig. 3. In these models, regime (*II*) is also identified, in which models display chemical stratification as a primordial layer with topography ("*T*") or post-overturn ROC layering ("$R_S$"; "$R_E$").

## D2   Rationale for main runs

The final bulk composition of the ambient (non-primordial) mantle ($f_{\text{bs,amb}}^{\text{final}}$) and related, the final amount of ROC heterogeneity that may form from the ambient mantle, depends on the fraction of primordial material that is processed in the upper mantle (melting) ($\chi_{\text{prim}}^{\text{pres}}$, see eq. (3) and Methods). In the test models discussed here, $f_{\text{bs,amb}}^{\text{final}}$ attains highly variable values, depending on $\chi_{\text{prim}}^{\text{pres}}$ (see Table E1). Models that display initial layering preservation (regime *II.T*), have an ambient mantle that is, relative to other models in this suite, most depleted as little primordial material is processed ($f_{\text{bs,amb}}^{\text{final}}<0.25$). For all other regimes, $B \leq 0.71$), moderate-to-much primordial material processing causes variably high $f_{\text{bs,amb}}^{\text{final}}$ (0.27-0.33), i.e., much higher than commonly assumed for Earth (0.2-0.25). The rationale for the main model suite is to have ambient mantle compositions (and therefore the potential of ROC heterogeneity formation) comparable with one another, and we systematically vary the initial primordial material volume (to lower values) to obtain a similar ambient mantle composition between the models.

## D3   Fitting ambient mantle composition

In order to compute $D_{\text{prim}}$ for the main numerical experiments, we rewrite eq. (3) within the following assumptions. First, we assume that the final volume of primordial material mixing depends primarily on the preservation factor of primordial material

33

and initial volume of primordial material:

$$V_{\text{prim,molten}}^{\text{final}} = V_{\text{prim}}^{\text{ini}} - V_{\text{prim}}^{\text{final}} = (1 - \chi_{\text{prim}}^{\text{pres}}) \cdot V_{\text{prim}}^{\text{ini}} \tag{D1}$$

with preserved primordial volume fraction $\chi_{\text{prim}}^{\text{pres}}$ ($= \frac{V_{\text{prim}}^{\text{final}}}{V_{\text{prim}}^{\text{ini}}}$). Secondly, for simplicity, we assume that the preservation factor $\chi_{\text{prim}}^{\text{pres}}$ remains roughly constant for a given set of physical parameters of primordial material (viscosity contrast $\lambda_{\text{prim}}$ and intrinsic buoyancy number $B$). Moreover, each experiment (set of $\lambda_{\text{prim}}$ and $B$), we set $\chi_{\text{prim}}^{\text{pres}}$ equal to the resulting final primordial heterogeneity volume ($\chi_{\text{prim}}^{\text{LM}}$ in Table E2) fraction from the same experiment in the test model suite. With these assumptions, we rewrite eq. (3) as:

$$f_{\text{bs,amb}}^{\text{final}} = \frac{f_{\text{bs,amb}}^{\text{ini}} \cdot \left(V_{\text{mantle}} - V_{\text{prim}}^{\text{ini}}\right) + c_{\text{bs,prim}} \cdot \left(1 - \chi_{\text{prim}}^{\text{pres}}\right) \cdot V_{\text{prim}}^{\text{ini}}}{V_{\text{mantle}} - \chi_{\text{prim}}^{\text{pres}} \cdot V_{\text{prim}}^{\text{ini}}} \tag{D2}$$

Alternatively, we can make $V_{\text{prim}}^{\text{ini}}$ dependent on $f_{\text{bs,amb}}^{\text{final}}$ by rewriting eq. (D2):

$$f_{\text{bs,amb}}^{\text{final}} \cdot V_{\text{mantle}} - f_{\text{bs,amb}}^{\text{final}} \cdot \chi_{\text{prim}}^{\text{pres}} \cdot V_{\text{prim}}^{\text{ini}} = f_{\text{bs,amb}}^{\text{ini}} \cdot V_{\text{mantle}} - f_{\text{bs,amb}}^{\text{ini}} \cdot V_{\text{prim}}^{\text{ini}} + c_{\text{bs,prim}} \cdot \left(1 - \chi_{\text{prim}}^{\text{pres}}\right) \cdot V_{\text{prim}}^{\text{ini}} \tag{D3}$$

$$f_{\text{bs,amb}}^{\text{ini}} \cdot V_{\text{prim}}^{\text{ini}} - f_{\text{bs,amb}}^{\text{final}} \cdot \chi_{\text{prim}}^{\text{pres}} \cdot V_{\text{prim}}^{\text{ini}} - c_{\text{bs,prim}} \cdot \left(1 - \chi_{\text{prim}}^{\text{pres}}\right) \cdot V_{\text{prim}}^{\text{ini}} = f_{\text{bs,amb}}^{\text{ini}} \cdot V_{\text{mantle}} - f_{\text{bs,amb}}^{\text{final}} \cdot V_{\text{mantle}} \tag{D4}$$

$$V_{\text{prim}}^{\text{ini}} \left(f_{\text{bs,ambt}}^{\text{ini}} - f_{\text{bs,amb}}^{\text{final}} \cdot \chi_{\text{prim}}^{\text{pres}} - c_{\text{bs,prim}} \cdot \left(1 - \chi_{\text{prim}}^{\text{pres}}\right)\right) = V_{\text{mantle}} \left(f_{\text{bs,amb}}^{\text{ini}} - f_{\text{bs,amb}}^{\text{final}}\right) \tag{D5}$$

leading to the expression for $V_{\text{prim}}^{\text{ini}}$:

$$V_{\text{prim}}^{\text{ini}} = V_{\text{mantle}} \frac{f_{\text{bs,amb}}^{\text{final}} - f_{\text{bs,amb}}^{\text{ini}}}{c_{\text{bs,prim}} \cdot \left(1 - \chi_{\text{prim}}^{\text{pres}}\right) + \chi_{\text{prim}}^{\text{pres}} \cdot f_{\text{bs,amb}}^{\text{final}} - f_{\text{bs,amb}}^{\text{ini}}} \tag{D6}$$

We use eq. (D6) and set the target ambient mantle composition on $f_{\text{bs,amb}}^{\text{final}} = 0.25$ to find $V_{\text{prim}}^{\text{ini}}$ (and hence $D_{\text{prim}}$) for each case. Note that since we use spherical annulus geometry, all volumes scale as in 3D spherical geometry (Hernlund and Tackley, 2008).

Following this approach, all main models display a final ambient mantle composition of $f_{\text{bs,amb}}^{\text{final}} = 0.24\text{-}0.26$ (Table E1) after 4.5 Gyr model time. This outcome demonstrates that the above assumptions are valid within reasonable margin.

## Appendix E: Summary of numerical experiments

Table E1: Model parameter summary and output quantities of models in the model suite discussed in the main text, averaged between 4.25 and 4.5 Gyr of model evolution. All models have a different $D_{\text{prim}}$, see text. Plateness $P$ and mobility $M$ from Tackley (2000).

| Model | $\lambda_{\text{prim}}$ | $B$ ($Mg\#$) | $D_{\text{prim}}$ [km] | $t_{\text{ot}}$ [Gyr] | $P$ | $M$ | $T_{\text{mean}}$ [K] | $\eta_{\text{av}}$ [Pa·s] | $f_{\text{bs,amb}}^{\text{final}}$ | $\chi_{\text{prim}}^{\text{pres}}$ [v%$_{\text{prim}}^{\text{ini}}$] | $\chi_{\text{prim}}^{\text{LM}}$ [v%$_{\text{LM}}$] | $\chi_{\text{ROC}}^{\text{LM}}$ [v%$_{\text{LM}}$] | regime |
|---|---|---|---|---|---|---|---|---|---|---|---|---|---|
| $M_{10\text{aD}}$ | 10 | 0.07 (0.90) | 1568 | 0.28 | 0.93 | 1.49 | 1935 | $2.1 \cdot 10^{24}$ | 0.26 | 1.7 | 1.0 | 6.9 | III.M |
| $M_{10\text{bD}}$ | 10 | 0.14 (0.89) | 1568 | 0.30 | 0.95 | 1.49 | 1984 | $8.1 \cdot 10^{23}$ | 0.26 | 2.5 | 1.5 | 5.7 | III.M |
| $M_{10\text{cD}}$ | 10 | 0.21 (0.89) | 1580 | 0.32 | 0.92 | 1.52 | 2011 | $1.3 \cdot 10^{24}$ | 0.25 | 2.6 | 1.6 | 6.1 | III.M |
| $M_{10\text{dD}}$ | 10 | 0.28 (0.88) | 1582 | 0.32 | 0.95 | 1.43 | 2021 | $1.1 \cdot 10^{24}$ | 0.25 | 2.1 | 1.3 | 7.1 | III.M |
| $M_{10\text{eD}}$ | 10 | 0.35 (0.88) | 1583 | 0.34 | 0.97 | 1.40 | 2087 | $9.3 \cdot 10^{23}$ | 0.25 | 3.0 | 1.8 | 6.0 | III.D |
| $M_{10\text{fD}}$ | 10 | 0.42 (0.87) | 1586 | 0.35 | 0.94 | 1.13 | 2115 | $8.5 \cdot 10^{23}$ | 0.25 | 3.3 | 2.0 | 5.7 | III.D |
| $M_{10\text{gD}}$ | 10 | 0.50 (0.87) | 1603 | 0.33 | 0.97 | 1.24 | 2186 | $9.3 \cdot 10^{23}$ | 0.26 | 3.9 | 2.4 | 4.2 | III.D |
| $M_{10\text{hD}}$ | 10 | 0.57 (0.86) | 1615 | 0.34 | 0.97 | 1.3 | 2218 | $7.2 \cdot 10^{23}$ | 0.26 | 6.8 | 4.2 | 3.4 | III.D |
| $M_{30\text{aD}}$ | 30 | 0.07 (0.90) | 1574 | 0.51 | 0.94 | 1.38 | 1999 | $6.9 \cdot 10^{23}$ | 0.25 | 1.8 | 1.1 | 4.0 | III.M |
| $M_{30\text{bD}}$ | 30 | 0.14 (0.89) | 1569 | 0.52 | 0.94 | 1.42 | 2063 | $5.7 \cdot 10^{23}$ | 0.25 | 1.7 | 1.0 | 4.5 | III.M |
| $M_{30\text{cD}}$ | 30 | 0.21 (0.89) | 1583 | 0.6 | 0.94 | 1.56 | 2063 | $9.0 \cdot 10^{23}$ | 0.25 | 6.6 | 4.0 | 5.3 | III.B |
| $M_{30\text{dD}}$ | 30 | 0.28 (0.88) | 1603 | 0.54 | 0.93 | 1.61 | 2090 | $8.7 \cdot 10^{23}$ | 0.25 | 8.1 | 5.0 | 5.8 | III.B |
| $M_{30\text{eD}}$ | 30 | 0.35 (0.88) | 1627 | 0.57 | 0.95 | 1.51 | 2150 | $8.2 \cdot 10^{23}$ | 0.25 | 3.8 | 2.4 | 5.5 | III.B |
| $M_{30\text{fD}}$ | 30 | 0.42 (0.87) | 1656 | 0.68 | 0.96 | 1.57 | 2202 | $5.8 \cdot 10^{23}$ | 0.25 | 4.9 | 3.2 | 4.2 | III.D |
| $M_{30\text{gD}}$ | 30 | 0.50 (0.87) | 1728 | 0.85 | 0.94 | 1.43 | 2214 | $4.6 \cdot 10^{23}$ | 0.26 | 5.2 | 3.7 | 2.8 | III.D |
| $M_{30\text{hD}}$ | 30 | 0.57 (0.86) | 1702 | 0.87 | 0.95 | 1.36 | 2194 | $5.5 \cdot 10^{23}$ | 0.25 | 7.5 | 5.2 | 3.8 | III.D |
| $M_{50\text{aD}}$ | 50 | 0.07 (0.90) | 1583 | 0.54 | 0.93 | 1.5 | 2034 | $5.6 \cdot 10^{23}$ | 0.25 | 3.7 | 2.3 | 3.6 | III.M |
| $M_{50\text{bD}}$ | 50 | 0.14 (0.89) | 1594 | 0.53 | 0.93 | 1.59 | 2085 | $5.1 \cdot 10^{23}$ | 0.25 | 7.7 | 4.8 | 5.3 | III.B |
| $M_{50\text{cD}}$ | 50 | 0.21 (0.89) | 1607 | 0.55 | 0.94 | 1.3 | 2110 | $7.3 \cdot 10^{23}$ | 0.25 | 13.0 | 8.1 | 4.8 | III.B |
| $M_{50\text{dD}}$ | 50 | 0.28 (0.88) | 1617 | 0.58 | 0.96 | 1.5 | 2130 | $7.6 \cdot 10^{23}$ | 0.25 | 7.6 | 4.7 | 5.8 | III.B |
| $M_{50\text{eD}}$ | 50 | 0.35 (0.88) | 1695 | 0.64 | 0.93 | 1.5 | 2171 | $5.5 \cdot 10^{23}$ | 0.25 | 13.2 | 8.8 | 5.5 | III.B |
| $M_{50\text{fD}}$ | 50 | 0.42 (0.87) | 1656 | 0.72 | 0.95 | 1.37 | 2210 | $5.1 \cdot 10^{23}$ | 0.25 | 12.8 | 8.3 | 3.4 | III.D |
| $M_{50\text{gD}}$ | 50 | 0.50 (0.87) | 1728 | 1 | 0.95 | 1.54 | 2192 | $4.7 \cdot 10^{23}$ | 0.25 | 15.1 | 10.4 | 2.0 | III.D |
| $M_{50\text{hD}}$ | 50 | 0.57 (0.86) | 1710 | 1.05 | 0.96 | 1.4 | 2180 | $6.7 \cdot 10^{23}$ | 0.25 | 18 | 12.1 | 2.2 | III.D |
| $M_{100\text{aD}}$ | 100 | 0.07 (0.90) | 1590 | 0.6 | 0.93 | 1.43 | 2036 | $6.1 \cdot 10^{23}$ | 0.25 | 9.2 | 5.6 | 4.0 | III.B |
| $M_{100\text{bD}}$ | 100 | 0.14 (0.89) | 1615 | 0.58 | 0.95 | 1.51 | 2105 | $6.3 \cdot 10^{23}$ | 0.24 | 16.1 | 10.1 | 4.0 | III.B |
| $M_{100\text{cD}}$ | 100 | 0.21 (0.89) | 1619 | 0.62 | 0.96 | 1.6 | 2161 | $5.7 \cdot 10^{23}$ | 0.24 | 23.7 | 14.9 | 4.4 | III.B |
| $M_{100\text{dD}}$ | 100 | 0.28 (0.88) | 1650 | 0.68 | 0.95 | 1.3 | 2212 | $6.2 \cdot 10^{23}$ | 0.24 | 23.7 | 15.3 | 3.4 | III.B |
| $M_{100\text{eD}}$ | 100 | 0.35 (0.88) | 1706 | 0.74 | 0.94 | 1.44 | 2222 | $4.9 \cdot 10^{23}$ | 0.25 | 15.8 | 10.7 | 2.5 | III.B |
| $M_{100\text{fD}}$ | 100 | 0.42 (0.87) | 1717 | 0.85 | 0.93 | 1.51 | 2204 | $4.1 \cdot 10^{23}$ | 0.25 | 18.6 | 12.7 | 2.2 | III.B |
| $M_{100\text{gD}}$ | 100 | 0.50 (0.87) | 1657 | 1.4 | 0.95 | 1.54 | 2189 | $5.4 \cdot 10^{23}$ | 0.24 | 32.2 | 20.9 | 1.3 | III.B |
| $M_{100\text{hD}}$ | 100 | 0.57 (0.86) | 1670 | 1.34 | 0.96 | 1.44 | 2101 | $7.8 \cdot 10^{23}$ | 0.25 | 34.1 | 22.3 | 1.2 | III.D |
| $M_{300\text{aD}}$ | 300 | 0.07 (0.90) | 1617 | 0.68 | 0.94 | 1.19 | 2105 | $5.6 \cdot 10^{23}$ | 0.25 | 13.3 | 8.3 | 3.0 | III.B |
| $M_{300\text{cD}}$ | 300 | 0.21 (0.89) | 1678 | 0.8 | 0.95 | 1.41 | 2185 | $6.4 \cdot 10^{23}$ | 0.24 | 35.6 | 23.5 | 3.1 | III.B |
| $M_{300\text{dD}}$ | 300 | 0.28 (0.88) | 1717 | 0.92 | 0.94 | 1.61 | 2194 | $6.1 \cdot 10^{23}$ | 0.24 | 35.5 | 24.2 | 2.5 | III.B |
| $M_{300\text{eD}}$ | 300 | 0.35 (0.88) | 1743 | 1.18 | 0.94 | 1.53 | 2167 | $4.2 \cdot 10^{23}$ | 0.24 | 35.3 | 24.6 | 2.0 | III.B |
| $M_{300\text{fD}}$ | 300 | 0.42 (0.87) | 1768 | 1.38 | 0.91 | 1.69 | 2105 | $5.6 \cdot 10^{23}$ | 0.25 | 32.1 | 22.8 | 1.3 | III.B |
| $M_{300\text{gD}}$ | 300 | 0.50 (0.87) | 1762 | 1.64 | 0.93 | 1.68 | 2025 | $6.1 \cdot 10^{23}$ | 0.24 | 36.2 | 25.6 | 1.4 | III.P |
| $M_{300\text{hD}}$ | 300 | 0.57 (0.86) | 1766 | 1.68 | 0.96 | 1.66 | 2052 | $7.5 \cdot 10^{23}$ | 0.26 | 43.3 | 32.6 | 1.3 | III.D |
| $M_{500\text{aD}}$ | 500 | 0.07 (0.90) | 1621 | 0.8 | 0.95 | 1.35 | 2068 | $6.3 \cdot 10^{23}$ | 0.25 | 12.3 | 7.7 | 3.5 | III.B |
| $M_{500\text{bD}}$ | 500 | 0.14 (0.89) | 1635 | 0.9 | 0.94 | 1.31 | 2127 | $5.7 \cdot 10^{23}$ | 0.24 | 25.3 | 16.1 | 2.7 | III.B |

| | | | | | | | | | | | | | |
|---|---|---|---|---|---|---|---|---|---|---|---|---|---|
| $M_{500\mathrm{cD}}$ | 500 | 0.21 (0.89) | 1699 | 1.02 | 0.95 | 1.69 | 2180 | $5.3\cdot10^{23}$ | 0.23 | 41.7 | 28.0 | 2.8 | III.B |
| $M_{500\mathrm{dD}}$ | 500 | 0.28 (0.88) | 1728 | 1.32 | 0.94 | 1.56 | 2172 | $6.3\cdot10^{23}$ | 0.24 | 38.9 | 26.8 | 2.5 | III.B |
| $M_{500\mathrm{eD}}$ | 500 | 0.35 (0.88) | 1762 | 1.48 | 0.92 | 1.51 | 2150 | $4.9\cdot10^{23}$ | 0.24 | 37.5 | 26.5 | 1.8 | III.B |
| $M_{500\mathrm{fD}}$ | 500 | 0.42 (0.87) | 1840 | 1.7 | 0.92 | 1.54 | 2084 | $5.7\cdot10^{23}$ | 0.25 | 38.5 | 29.0 | 2.3 | III.B |
| $M_{500\mathrm{gD}}$ | 500 | 0.50 (0.87) | 1844 | 2 | 0.93 | 1.71 | 2012 | $9.1\cdot10^{23}$ | 0.24 | 44.0 | 33.2 | 1.4 | III.P |
| $M_{500\mathrm{hD}}$ | 500 | 0.57 (0.86) | 1848 | 2.05 | 0.94 | 1.72 | 2032 | $8.8\cdot10^{23}$ | 0.25 | 48.0 | 36.1 | 1.1 | III.D |
| $M^{B0}_{50\mathrm{dD}}$ | 50 | 0.28 (0.88) | 1539 | 0.55 | 0.95 | 1.62 | 2108 | $6.2\cdot10^{23}$ | 0.30 | 42 | 26.3 | 4.7 | III.B |
| $M^{B1}_{50\mathrm{dD}}$ | 50 | 0.28 (0.88) | 1514 | 0.57 | 0.94 | 1.44 | 2059 | $1.2\cdot10^{24}$ | 0.30 | 37.7 | 23.7 | 6.7 | III.B |
| $M^{B0}_{100\mathrm{dD}}$ | 100 | 0.28 (0.88) | 1571 | 0.70 | 0.94 | 1.52 | 2101 | $6.3\cdot10^{23}$ | 0.30 | 41.5 | 27.0 | 4.1 | III.B |
| $M^{B1}_{100\mathrm{dD}}$ | 100 | 0.28 (0.88) | 1546 | 0.72 | 0.95 | 1.64 | 2038 | $1.1\cdot10^{24}$ | 0.30 | 43.4 | 28.2 | 6.3 | III.B |
| $M^{B2}_{100\mathrm{dD}}$ | 100 | 0.28 (0.88) | 1521 | 0.76 | 0.92 | 1.80 | 2039 | $1.5\cdot10^{24}$ | 0.30 | 40 | 26.1 | 8.7 | III.B |

[B0-2] stands for additional ancient FeO-rich ancient layer on top of the CMB, with layer thickness 150 ([B0]), 200 ([B1]) and 250 ([B2]) km, respectively.

Table E2: Model parameter summary and output quantities, averaged between 4.25 and 4.5 Gyr of model evolution. Models in this table belong to the test model suite ($D_\mathrm{prim}$ fixed to 2230 km, see Appendix D). Plateness $P$ and mobility $M$ from Tackley (2000); * denotes the reference model.

| Model | $\lambda_\mathrm{prim}$ | $B\ (Mg\#)$ | $D_\mathrm{prim}$ [km] | $t_\mathrm{ot}$ [Gyr] | $P$ | $M$ | $T_\mathrm{mean}$ [K] | $\eta_\mathrm{av}$ [Pa·s] | $f_\mathrm{bs,amb}^\mathrm{final}$ | $\chi_\mathrm{prim}^\mathrm{LM}$ [v%$_\mathrm{LM}$] | $\chi_\mathrm{ROC}^\mathrm{LM}$ [v%$_\mathrm{LM}$] | regime |
|---|---|---|---|---|---|---|---|---|---|---|---|---|
| $M_\mathrm{10a}$ | 10 | 0.07 (0.9) | 2230 | 0.24 | 0.25 | 0.01 | 1975 | $7.0\cdot10^{24}$ | 0.32 | 0.0 | 11.2 | II.R$_\mathrm{S}$ |
| $M_\mathrm{10b}$ | 10 | 0.14 (0.89) | 2230 | 0.24 | 0.27 | 0.01 | 1967 | $6.9\cdot10^{24}$ | 0.32 | 0.1 | 10.5 | II.R$_\mathrm{S}$ |
| $M_\mathrm{10c}$ | 10 | 0.21 (0.89) | 2230 | 0.25 | 0.96 | 1.35 | 1963 | $9.8\cdot10^{23}$ | 0.31 | 1.8 | 6.4 | III.M |
| $M_\mathrm{10d}$ | 10 | 0.28 (0.88) | 2230 | 0.27 | 0.96 | 1.31 | 2061 | $9.0\cdot10^{23}$ | 0.31 | 2.1 | 5.2 | III.M |
| $M_\mathrm{10e}$ | 10 | 0.35 (0.88) | 2230 | 0.27 | 0.94 | 1,52 | 2084 | $5.6\cdot10^{23}$ | 0.30 | 2.2 | 5.3 | III.M |
| $M_\mathrm{10f}$ | 10 | 0.42 (0.87) | 2230 | 0.28 | 0.92 | 1.18 | 2133 | $7.9\cdot10^{23}$ | 0.29 | 2.6 | 5.8 | III.D |
| $M_\mathrm{10g}$ | 10 | 0.50 (0.87) | 2230 | 0.38 | 0.93 | 1.51 | 2179 | $7.8\cdot10^{23}$ | 0.29 | 5.3 | 5.0 | III.D |
| $M_\mathrm{10h}$ | 10 | 0.57 (0.86) | 2230 | 0.4 | 0.92 | 1.46 | 2205 | $6.5\cdot10^{23}$ | 0.28 | 7.0 | 4.6 | III.D |
| $M_\mathrm{10i}$ | 10 | 0.64 (0.86) | 2230 | 0.88 | 0.91 | 1.25 | 2184 | $6.1\cdot10^{23}$ | 0.23 | 31.3 | 4.2 | III.P |
| $M_\mathrm{10j}$ | 10 | 0.71 (0.85) | 2230 | 1.17 | 0.91 | 1.2 | 2190 | $4.9\cdot10^{23}$ | 0.24 | 33.6 | 3.6 | III.P |
| $M_\mathrm{10k}$ | 10 | 0.78 (0.85) | 2230 | - | 0.92 | 0.98 | 2235 | $3.8\cdot10^{23}$ | 0.23 | 47.7 | 2.0 | II.T |
| $M_\mathrm{30a}$ | 30 | 0.07 (0.9) | 2230 | 0.40 | 0.95 | 1.53 | 1930 | $3.2\cdot10^{24}$ | 0.32 | 1.1 | 9.3 | II.R$_\mathrm{E}$ |
| $M_\mathrm{30b}$ | 30 | 0.14 (0.89) | 2230 | 0.40 | 0.95 | 1.22 | 1934 | $2\cdot10^{24}$ | 0.32 | 2.0 | 7.7 | II.R$_\mathrm{E}$ |
| $M_\mathrm{30c}$ | 30 | 0.21 (0.89) | 2230 | 0.44 | 0.94 | 1.36 | 1992 | $6.4\cdot10^{23}$ | 0.32 | 2.8 | 4.8 | III.M |
| $M_\mathrm{30d}$ | 30 | 0.28 (0.88) | 2230 | 0.50 | 0.94 | 1.11 | 2078 | $6.7\cdot10^{23}$ | 0.31 | 5.0 | 4.2 | III.B |
| $M_\mathrm{30e}$ | 30 | 0.35 (0.88) | 2230 | 0.65 | 0.97 | 1.33 | 2130 | $6.1\cdot10^{23}$ | 0.31 | 9.2 | 4.1 | III.B |
| $M_\mathrm{30f}$ | 30 | 0.42 (0.87) | 2230 | 0.80 | 0.95 | 1.44 | 2150 | $5.5\cdot10^{23}$ | 0.31 | 13.3 | 3.9 | III.B |
| $M_\mathrm{30g}$ | 30 | 0.50 (0.87) | 2230 | 1.00 | 0.95 | 1.63 | 2177 | $4.7\cdot10^{23}$ | 0.30 | 23.8 | 3.4 | III.B |
| $M_\mathrm{30h}$ | 30 | 0.57 (0.86) | 2230 | 1.22 | 0.92 | 1.55 | 2180 | $4.2\cdot10^{23}$ | 0.30 | 28.5 | 2.2 | III.B |
| $M_\mathrm{30i}$ | 30 | 0.64 (0.86) | 2230 | 1.48 | 0.94 | 1.40 | 2103 | $6.8\cdot10^{23}$ | 0.29 | 32.8 | 3.0 | III.P |
| $M_\mathrm{30j}$ | 30 | 0.71 (0.85) | 2230 | 1.70 | 0.91 | 1.41 | 2110 | $1.4\cdot10^{24}$ | 0.26 | 56.0 | 3.0 | III.P |
| $M_\mathrm{30k}$ | 30 | 0.78 (0.85) | 2230 | - | 0.92 | 1.04 | 2168 | $2.3\cdot10^{24}$ | 0.24 | 70.3 | 1.8 | II.T |
| $M_\mathrm{50a}$ | 50 | 0.07 (0.90) | 2230 | 0.58 | 0.96 | 1.38 | 1955 | $3.4\cdot10^{24}$ | 0.32 | 1.9 | 7.7 | II.R$_\mathrm{E}$ |
| $M_\mathrm{50b}$ | 50 | 0.14 (0.89) | 2230 | 0.58 | 0.95 | 1.22 | 1936 | $2\cdot10^{24}$ | 0.31 | 4.7 | 7.0 | II.R$_\mathrm{E}$ |
| $M_\mathrm{50c}$ | 50 | 0.21 (0.89) | 2230 | 0.57 | 0.93 | 1.62 | 1941 | $1.2\cdot10^{24}$ | 0.31 | 4.8 | 6.1 | III.M |
| $M_\mathrm{50d}$ | 50 | 0.28 (0.88) | 2230 | 0.58 | 0.94 | 1.36 | 2116 | $5.5\cdot10^{23}$ | 0.31 | 11.3 | 3.5 | III.B |
| $M_\mathrm{50e}$ | 50 | 0.35 (0.88) | 2230 | 0.62 | 0.96 | 1.31 | 2142 | $6.2\cdot10^{23}$ | 0.30 | 17.5 | 4.3 | III.B |
| $M_\mathrm{50f}$ | 50 | 0.42 (0.87) | 2230 | 0.62 | 0.95 | 1.40 | 2177 | $5.5\cdot10^{23}$ | 0.31 | 14.3 | 3.3 | III.B |
| $M_\mathrm{50g}$ | 50 | 0.50 (0.87) | 2230 | 0.65 | 0.95 | 1.33 | 2127 | $5.3\cdot10^{23}$ | 0.30 | 18.2 | 2.9 | III.B |
| $M_\mathrm{50h}$ | 50 | 0.57 (0.86) | 2230 | 0.75 | 0.93 | 1.45 | 2132 | $4.6\cdot10^{23}$ | 0.30 | 20.6 | 2.0 | III.B |
| $M_\mathrm{50i}$ | 50 | 0.64 (0.86) | 2230 | 1.20 | 0.92 | 1.47 | 2105 | $7.7\cdot10^{23}$ | 0.28 | 40.5 | 2.6 | III.P |
| $M_\mathrm{50j}$ | 50 | 0.71 (0.85) | 2230 | 1.45 | 0.91 | 1.11 | 2043 | $2.2\cdot10^{24}$ | 0.26 | 58.2 | 3.1 | III.P |
| $M_\mathrm{50k}$ | 50 | 0.78 (0.85) | 2230 | - | 0.94 | 1.17 | 2155 | $2.4\cdot10^{24}$ | 0.23 | 74.5 | 1.7 | II.T |
| $M_\mathrm{100a}$ | 100 | 0.07 (0.90) | 2230 | 0.89 | 0.94 | 1.43 | 1935 | $2.5\cdot10^{24}$ | 0.31 | 4.2 | 7.1 | II.R$_\mathrm{E}$ |
| $M_\mathrm{100b}$ | 100 | 0.14 (0.89) | 2230 | 0.90 | 0.96 | 1.20 | 1960 | $2.2\cdot10^{24}$ | 0.31 | 7.3 | 5.5 | III.B |
| $M_\mathrm{100c}$ | 100 | 0.21 (0.89) | 2230 | 0.90 | 0.94 | 1.36 | 2085 | $5.3\cdot10^{23}$ | 0.31 | 12.1 | 3.1 | III.B |
| **$M_\mathrm{100d}$ \*** | **100** | **0.28 (0.88)** | **2230** | **0.90** | **0.94** | **1.45** | **2105** | **$4.9\cdot10^{23}$** | **0.31** | **15.1** | **3.4** | **III.B** |

| | | | | | | | | | | | | |
|---|---|---|---|---|---|---|---|---|---|---|---|---|
| $M_{100e}$ | 100 | 0.35 (0.88) | 2230 | 0.92 | 0.94 | 1.38 | 2142 | $5.1 \cdot 10^{23}$ | 0.30 | 18.6 | 3.3 | III.B |
| $M_{100f}$ | 100 | 0.42 (0.87) | 2230 | 0.95 | 0.95 | 1.75 | 2156 | $5.3 \cdot 10^{23}$ | 0.30 | 20.9 | 3.1 | III.B |
| $M_{100g}$ | 100 | 0.50 (0.87) | 2230 | 1.07 | 0.93 | 1.50 | 2114 | $3.8 \cdot 10^{23}$ | 0.31 | 15.9 | 2.5 | III.B |
| $M_{100h}$ | 100 | 0.57 (0.86) | 2230 | 1.20 | 0.94 | 1.43 | 2109 | $5.2 \cdot 10^{23}$ | 0.30 | 18.0 | 1.9 | III.B |
| $M_{100i}$ | 100 | 0.64 (0.86) | 2230 | 1.65 | 0.90 | 1.56 | 1957 | $1.5 \cdot 10^{24}$ | 0.29 | 34.9 | 3.5 | III.P |
| $M_{100j}$ | 100 | 0.71 (0.85) | 2230 | 1.70 | 0.93 | 1.41 | 2009 | $2.9 \cdot 10^{24}$ | 0.27 | 55.5 | 2.7 | III.P |
| $M_{100k}$ | 100 | 0.78 (0.85) | 2230 | - | 0.94 | 1.20 | 2152 | $2.6 \cdot 10^{24}$ | 0.22 | 78.5 | 1.5 | II.T |
| $M_{300a}$ | 300 | 0.07 (0.90) | 2230 | 1.48 | 0.92 | 1.56 | 1949 | $1.8 \cdot 10^{24}$ | 0.31 | 7.8 | 5.3 | III.B |
| $M_{300b}$ | 300 | 0.14 (0.89) | 2230 | 1.48 | 0.96 | 1.37 | 1965 | $1.3 \cdot 10^{24}$ | 0.31 | 9.1 | 5.2 | III.B |
| $M_{300c}$ | 300 | 0.21 (0.89) | 2230 | 1.48 | 0.94 | 1.45 | 2048 | $6.4 \cdot 10^{23}$ | 0.31 | 15.3 | 3.2 | III.B |
| $M_{300d}$ | 300 | 0.28 (0.88) | 2230 | 1.48 | 0.94 | 1.42 | 2178 | $5.7 \cdot 10^{23}$ | 0.30 | 22.9 | 2.5 | III.B |
| $M_{300e}$ | 300 | 0.35 (0.88) | 2230 | 1.50 | 0.95 | 1.69 | 2161 | $5.4 \cdot 10^{23}$ | 0.30 | 23.8 | 2.1 | III.B |
| $M_{300f}$ | 300 | 0.42 (0.87) | 2230 | 1.50 | 0.92 | 1.57 | 2084 | $5 \cdot 10^{23}$ | 0.30 | 25.9 | 3.0 | III.B |
| $M_{300g}$ | 300 | 0.50 (0.87) | 2230 | 1.50 | 0.90 | 1.48 | 2021 | $4.9 \cdot 10^{23}$ | 0.30 | 25.5 | 2.7 | III.B |
| $M_{300h}$ | 300 | 0.57 (0.86) | 2230 | 1.52 | 0.90 | 1.59 | 1936 | $8.3 \cdot 10^{23}$ | 0.30 | 27.3 | 4.2 | III.P |
| $M_{300i}$ | 300 | 0.64 (0.86) | 2230 | 1.56 | 0.92 | 1.81 | 1935 | $3 \cdot 10^{24}$ | 0.28 | 43.0 | 3.8 | III.P |
| $M_{300j}$ | 300 | 0.71 (0.85) | 2230 | - | 0.92 | 1.19 | 2022 | $3.6 \cdot 10^{24}$ | 0.25 | 63.8 | 2.8 | II.T |
| $M_{300k}$ | 300 | 0.78 (0.85) | 2230 | - | 0.94 | 1.41 | 2177 | $3.9 \cdot 10^{24}$ | 0.21 | 85.0 | 0.66 | II.T |
| $M_{500a}$ | 500 | 0.07 (0.90) | 2230 | 2.00 | 0.96 | 1.38 | 1935 | $2 \cdot 10^{4}$ | 0.31 | 8.6 | 5.6 | III.B |
| $M_{500b}$ | 500 | 0.14 (0.89) | 2230 | 2.00 | 0.94 | 1.49 | 1979 | $9.6 \cdot 10^{23}$ | 0.31 | 10.1 | 3.8 | III.B |
| $M_{500c}$ | 500 | 0.21 (0.89) | 2230 | 2.00 | 0.93 | 1.41 | 2082 | $5.3 \cdot 10^{23}$ | 0.31 | 17.2 | 3.0 | III.B |
| $M_{500d}$ | 500 | 0.28 (0.88) | 2230 | 2.00 | 0.93 | 1.28 | 2091 | $5.9 \cdot 10^{23}$ | 0.30 | 22.1 | 3.2 | III.B |
| $M_{500e}$ | 500 | 0.35 (0.88) | 2230 | 2.00 | 0.94 | 1.53 | 2139 | $5.4 \cdot 10^{23}$ | 0.30 | 24.7 | 2.5 | III.B |
| $M_{500f}$ | 500 | 0.42 (0.87) | 2230 | 2.03 | 0.92 | 1.57 | 2062 | $7.9 \cdot 10^{23}$ | 0.29 | 31.9 | 3.0 | III.B |
| $M_{500g}$ | 500 | 0.50 (0.87) | 2230 | 2.05 | 0.93 | 1.51 | 2001 | $1 \cdot 10^{24}$ | 0.29 | 34.5 | 3.6 | III.P |
| $M_{500h}$ | 500 | 0.57 (0.86) | 2230 | 2.10 | 0.91 | 1.64 | 1989 | $1.9 \cdot 10^{24}$ | 0.28 | 46.7 | 3.6 | III.P |
| $M_{500i}$ | 500 | 0.64 (0.86) | 2230 | 2.10 | 0.92 | 1.88 | 2061 | $3.6 \cdot 10^{24}$ | 0.24 | 69.7 | 1.6 | III.P |
| $M_{500j}$ | 500 | 0.71 (0.85) | 2230 | - | 0.94 | 1.59 | 1084 | $5 \cdot 10^{23}$ | 0.23 | 75.0 | 1.7 | II.T |
| $M_{500k}$ | 500 | 0.78 (0.85) | 2230 | - | 0.93 | 1.23 | 2167 | $5 \cdot 10^{23}$ | 0.20 | 86.2 | 0.5 | II.T |

*Author contributions.* A.G. designed the study, conducted the experiments, interpreted the results, and prepared this manuscript. M.B. contributed to the study design and interpretation of the results. P.T. designed the 3D thermomechanical code and contributed to results interpretation. All authors collaborated and contributed intellectually to this paper.

655    *Competing interests.* The authors declare no competing interests.

39

# References

Allegre, C. J. and Turcotte, D. L.: Implications of a two-component marble-cake mantle, Nature, 323, 123–127, 1986.

Andrault, D., Muñoz, M., Pesce, G., Cerantola, V., Chumakov, A., Kantor, I., Pascarelli, S., Rüffer, R., and Hennet, L.: Large oxygen excess in the primitive mantle could be the source of the Great Oxygenation Event, Geochemical Perspectives Letters, 6, 5–10, https://doi.org/10.7185/geochemlet.1801, 2017.

Armstrong, K., Frost, D. J., McCammon, C. A., Rubie, D. C., and Ballaran, T. B.: Deep magma ocean formation set the oxidation state of Earth's mantle, Science, 365, 903–906, https://doi.org/10.1126/science.aax8376, 2019.

Badro, J., Siebert, J., and Nimmo, F.: An early geodynamo driven by exsolution of mantle components from Earth's core, Nature, 536, 326–328, https://doi.org/10.1038/nature18594, 2016.

Ballmer, M. D., Schmerr, N. C., Nakagawa, T., and Ritsema, J.: Compositional mantle layering revealed by slab stagnation at 1000-km depth, Science Advances, 1, 1–10, https://doi.org/10.1126/sciadv.1500815, 2015.

Ballmer, M. D., Schumacher, L., Lekic, V., Thomas, C., and Ito, G.: Compositional layering within the large low shear-wave velocity provinces in the lower mantle, Geochemistry Geophysics Geosystems, 17, 5056–5077, https://doi.org/10.1002/2016GC006605, 2016.

Ballmer, M. D., Houser, C., Hernlund, J. W., Wentzcovitch, R. M., and Hirose, K.: Persistence of strong silica-enriched domains in the Earth's lower mantle, Nature Geoscience, 10, 236–240, https://doi.org/10.1038/ngeo2898, 2017a.

Ballmer, M. D., Lourenço, D. L., Hirose, K., Caracas, R., and Nomura, R.: Reconciling magma-ocean crystallization models with the present-day structure of the Earth's mantle, Geochemistry, Geophysics, Geosystems, 18, 1–26, https://doi.org/10.1002/2017GC006917, 2017b.

Becker, T. W., Kellogg, J. B., and O'Connell, R. J.: Thermal constraints on the survival of primitive blobs in the lower mantle, Earth and Planetary Science Letters, 171, 351–365, https://doi.org/10.1016/S0012-821X(99)00160-0, 1999.

Bédard, J. H.: Stagnant lids and mantle overturns: Implications for Archaean tectonics, magmagenesis, crustal growth, mantle evolution, and the start of plate tectonics, Geoscience Frontiers, 9, 19–49, https://doi.org/10.1016/j.gsf.2017.01.005, 2018.

Boukaré, C., Ricard, Y., and Fiquet, G.: Thermodynamics of the MgO-FeO-SiO2 system up to 140 GPa: Application to the crystallization of Earth's magma ocean, Journal of Geophysical Research: Solid Earth, 120, 6085–6101, https://doi.org/10.1002/2015JB011929, 2015.

Bower, D. J., Gurnis, M., and Seton, M.: Lower mantle structure from paleogeographically constrained dynamic Earth models, Geochemistry, Geophysics, Geosystems, 14, 44–63, https://doi.org/10.1029/2012GC004267, 2013.

Brown, S. M., Elkins-Tanton, L. T., and Walker, R. J.: Effects of magma ocean crystallization and overturn on the development of142Nd and182W isotopic heterogeneities in the primordial mantle, Earth and Planetary Science Letters, 408, 319–330, https://doi.org/10.1016/j.epsl.2014.10.025, http://dx.doi.org/10.1016/j.epsl.2014.10.025, 2014.

Cabral, R. A., Jackson, M. G., Rose-Koga, E. F., Koga, K. T., Whitehouse, M. J., Antonelli, M. A., Farquhar, J., Day, J. M., and Hauri, E. H.: Anomalous sulphur isotopes in plume lavas reveal deep mantle storage of Archaean crust, Nature, 496, 490–493, https://doi.org/10.1038/nature12020, 2013.

Caracas, R., Hirose, K., Nomura, R., and Ballmer, M. D.: Melt-crystal density crossover in a deep magma ocean, Earth and Planetary Science Letters, 516, 202–211, https://doi.org/10.3929/ethz-a-010782581, 2019.

Chauvel, C., Hofmann, A. W., and Vidal, P.: himu-em: The French Polynesian connection, Earth and Planetary Science Letters, 110, 99–119, https://doi.org/10.1016/0012-821X(92)90042-T, 1992.

Christensen, U. R. and Hofmann, A. W.: Segregation of subducted oceanic crust in the convecting mantle, Journal of Geophysical Research, 99, https://doi.org/10.1029/93jb03403, 1994.

Coltice, N. and Schmalzl, J.: Mixing times in the mantle of the early Earth derived from 2-D and 3-D numerical simulations of convection, Geophysical Research Letters, 33, 5–8, https://doi.org/10.1029/2006GL027707, 2006.

Condie, K. C.: A planet in transition: The onset of plate tectonics on Earth between 3 and 2 Ga?, Geoscience Frontiers, 9, 51–60, https://doi.org/10.1016/j.gsf.2016.09.001, 2018.

Corgne, A., Liebske, C., Wood, B. J., Rubie, D. C., and Frost, D. J.: Silicate perovskite-melt partitioning of trace elements and geochemical signature of a deep perovskitic reservoir, Geochimica et Cosmochimica Acta, 69, 485–496, https://doi.org/10.1016/j.gca.2004.06.041, 2005.

Crameri, F.: Scientific colour-maps, http://doi.org/10.5281/zenodo.1243862, 2018.

Crameri, F. and Tackley, P. J.: Spontaneous development of arcuate single-sided subduction in global 3-D mantle convection models with a free surface, Journal of Geophysical Research: Solid Earth, 119, 5921–5942, https://doi.org/10.1002/2014JB010939, 2014.

Crowhurst, J. C., Brown, J. M., Goncharov, A. F., and Jacobsen, S. D.: Elasticity of (Mg ,Fe)O Through the Spin Transition of Iron in the Lower Mantle, Science, 319, 451–453, 2008.

Davaille, A.: Two-layer thermal convection in miscible viscous fluids, Journal of Fluid Mechanics, 379, 223–253, https://doi.org/10.1017/S0022112098003322, 1999.

Davies, G. F.: Comment on "Mixing by time-dependent convection" by U. Christensen, Earth and Planetary Science Letters, 98, 405–407, https://doi.org/10.1016/0012-821X(90)90041-U, 1990.

Davies, G. F.: Thermal Evolution of the Mantle, Treatise on Geophysics, 9, 197–216, https://doi.org/10.1016/B978-044452748-6.00145-0, 2007.

Deng, H., Ballmer, M. D., Reinhardt, C., Meier, M. M. M., Mayer, L., Stadel, J., and Benitez, F.: Primordial Earth Mantle Heterogeneity Caused by the Moon-forming Giant Impact?, The Astrophysical Journal, 887, 211, https://doi.org/10.3847/1538-4357/ab50b9, 2019.

Deschamps, F., Li, Y., and Tackley, P. J.: Large-Scale Thermo-chemical Structure of the Deep Mantle: Observations and Models, in: The Earth's Heterogeneous Mantle: A Geophysical, Geodynamical, and Geochemical Perspective, edited by Khan, A. and Deschamps, F., April, chap. 15, pp. 1–530, Springer, https://doi.org/10.1007/978-3-319-15627-9, 2015.

Dziewonski, A. M., Lekic, V., and Romanowicz, B. A.: Mantle Anchor Structure: An argument for bottom up tectonics, Earth and Planetary Science Letters, 299, 69–79, https://doi.org/10.1016/j.epsl.2010.08.013, 2010.

Elkins-Tanton, L. T.: Linked magma ocean solidification and atmospheric growth for Earth and Mars, Earth and Planetary Science Letters, 271, 181–191, https://doi.org/10.1016/j.epsl.2008.03.062, 2008.

Elkins-Tanton, L. T., Parmentier, E. M., and Hess, P. C.: Magma ocean fractional crystallization and cumulate overturn in terrestrial planets: Implications for Mars, Meteoritics and Planetary Science, 38, 1753–1771, https://doi.org/10.1111/j.1945-5100.2003.tb00013.x, 2003.

Ferrachat, S. and Ricard, Y.: Regular vs. chaotic mantle mixing, Earth and Planetary Science Letters, 155, 75–86, 1998.

Foley, B. J.: The dependence of planetary tectonics on mantle thermal state: Applications to early Earth evolution, Philosophical Transactions of the Royal Society A: Mathematical, Physical and Engineering Sciences, 376, https://doi.org/10.1098/rsta.2017.0409, 2018.

French, S. W. and Romanowicz, B.: Broad plumes rooted at the base of the Earth's mantle beneath major hotspots, Nature, 525, 95–99, https://doi.org/10.1038/nature14876, 2015.

Frost, D. J. and McCammon, C. A.: The Redox State of earth's mantle, Annual Review of Earth and Planetary Sciences, 36, 389–420, https://doi.org/10.1146/annurev.earth.36.031207.124322, 2008.

Fukao, Y. and Obayashi, M.: Subducted slabs stagnant above, penetrating through, and trapped below the 660 km discontinuity, Journal of Geophysical Research: Solid Earth, 118, 5920–5938, https://doi.org/10.1002/2013JB010466, 2013.

Gamal El Dien, H., Doucet, L. S., Murphy, J. B., and Li, Z. X.: Geochemical evidence for a widespread mantle re-enrichment 3.2 billion years ago: implications for global-scale plate tectonics, Scientific Reports, 10, 1–7, https://doi.org/10.1038/s41598-020-66324-y, 2020.

Girard, J., Amulele, G., Farla, R., Mohiuddin, A., and Karato, S. I.: Shear deformation of bridgmanite and magnesiowüstite aggregates at 740    lower mantle conditions, Science, 351, 144–147, https://doi.org/10.1126/science.aad3113, 2016.

Gonnermann, H. M. and Mukhopadhyay, S.: Non-equilibrium degassing and a primordial source for helium in ocean-island volcanism, Nature, 449, 1037–1040, https://doi.org/10.1038/nature06240, 2007.

Gülcher, A. J., Gebhardt, D. J., Ballmer, M. D., and Tackley, P. J.: Variable dynamic styles of primordial heterogeneity preservation in the Earth's lower mantle, Earth and Planetary Sciences Letters, 536, https://doi.org/10.1016/j.epsl.2020.116160, 2020.

745    Gülcher, A. J. P.: Coupled dynamics and evolution of primordial and recycled heterogeneity in Earth's lower mantle - Supplementary Videos, https://doi.org/10.5281/zenodo.4767426, https://doi.org/10.5281/zenodo.4767426, 2021.

Hansen, U. and Yuen, D. A.: Numerical simulations of thermal-chemical instabilities at the core-mantle boundary, Nature, 334, 237–240, 1988.

Helffrich, G. R., Ballmer, M. D., and Hirose, K.: Core-Exsolved SiO2 Dispersal in the Earth's Mantle, Journal of Geophysical Research: 750    Solid Earth, 123, 176–188, https://doi.org/10.1002/2017JB014865, 2018a.

Helffrich, G. R., Shahar, A., and Hirose, K.: Isotopic signature of core-derived SiO2, American Mineralogist, 103, 1161–1164, https://doi.org/10.2138/am-2018-6482CCBYNCND, 2018b.

Hernlund, J. W. and Houser, C.: On the statistical distribution of seismic velocities in Earth's deep mantle, Earth and Planetary Science Letters, 265, 423–437, https://doi.org/10.1016/j.epsl.2007.10.042, 2008.

755    Hernlund, J. W. and Tackley, P. J.: Modeling mantle convection in the spherical annulus, Physics of the Earth and Planetary Interiors, 171, 48–54, https://doi.org/10.1016/j.pepi.2008.07.037, 2008.

Herzberg, C. and Rudnick, R.: Formation of cratonic lithosphere: An integrated thermal and petrological model, Lithos, 149, 4–15, https://doi.org/10.1016/j.lithos.2012.01.010, 2012.

Herzberg, C., Condie, K., and Korenaga, J.: Thermal history of the Earth and its petrological expression, Earth and Planetary Science Letters, 760    292, 79–88, https://doi.org/10.1016/j.epsl.2010.01.022, 2010.

Hirose, K., Takafuji, N., Sata, N., and Ohishi, Y.: Phase transition and density of subducted MORB crust in the lower mantle, Earth and Planetary Science Letters, 237, 239–251, https://doi.org/10.1016/j.epsl.2005.06.035, 2005.

Hirose, K., Morard, G., Sinmyo, R., Umemoto, K., Hernlund, J. W., Helffrich, G. R., and Labrosse, S.: Crystallization of silicon dioxide and compositional evolution of the Earth's core, Nature, 543, 99–102, https://doi.org/10.1038/nature21367, 2017.

765    Hirth, G. and Kohlstedt, D. L.: The rheology of the upper mantle wedge: a view from experimentalists, in: The subduction Factory, edited by Eiler, J., American Geophysical Union, Washington D.C., 2003.

Hofmann, A. W.: Mantle geochemistry: The message from oceanic volcanism, Nature, 385, 218–229, https://doi.org/10.1038/385218a0, 1997.

Ito, E. and Takahashi, E.: Melting of peridotite at uppermost lower-mantle conditions, Nature, 328, 514–517, 770    https://doi.org/10.1038/328514a0, 1987.

Ito, E. and Takahashi, E.: Postspinel transformations in the system Mg2SiO4-Fe2SiO4 and some geophysical implications, Journal of Geophysical Research, 94, 10 637–10 646, 1989.

Jackson, M. G., Carlson, R. W., Kurz, M. D., Kempton, P. D., Francis, D., and Blusztajn, J.: Evidence for the survival of the oldest terrestrial mantle reservoir, Nature, 466, 853–856, https://doi.org/10.1038/nature09287, 2010.

775    Jenkins, J., Deuss, A., and Cottaar, S.: Converted phases from sharp 1000 km depth mid-mantle heterogeneity beneath Western Europe, Earth and Planetary Science Letters, 459, 196–207, https://doi.org/10.1016/j.epsl.2016.11.031, 2017.

Kaminski, E. and Javoy, M.: A two-stage scenario for the formation of the Earth's mantle and core, Earth and Planetary Science Letters, 365, 97–107, https://doi.org/10.1016/j.epsl.2013.01.025, 2013.

Karato, S. I. and Wu, P.: Rheology of the upper mantle: A synthesis, Science, 260, 771–778, https://doi.org/10.1126/science.260.5109.771,
780    1993.

Kawai, K., Tsuchiya, T., Tsuchiya, J., and Maruyama, S.: Lost primordial continents, Gondwana Research, 16, 581–586, https://doi.org/10.1016/j.gr.2009.05.012, 2009.

Kellogg, L. H., Hager, B. H., and van der Hilst, R. D.: Compositional Stratification in the Deep mantle, An Introduction to Celestial Mechanics, 283, 1881–1884, www.sciencemag.org, 1999.

785    Kleine, T., Touboul, M., Bourdon, B., Nimmo, F., Mezger, K., Palme, H., Jacobsen, S. B., Yin, Q. Z., and Halliday, A. N.: Hf-W chronology of the accretion and early evolution of asteroids and terrestrial planets, Geochimica et Cosmochimica Acta, 73, 5150–5188, https://doi.org/10.1016/j.gca.2008.11.047, 2009.

Korenaga, J.: Initiation and evolution of plate tectonics on earth: Theories and observations, Annual Review of Earth and Planetary Sciences, 41, 117–151, https://doi.org/10.1146/annurev-earth-050212-124208, 2013.

790    Labrosse, S., Hernlund, J. W., and Coltice, N.: A crystallizing dense magma ocean at the base of the Earth's mantle, Nature, 450, 866–869, https://doi.org/10.1038/nature06355, 2007.

Lenardic, A.: The diversity of tectonic modes and thoughts about transitions between them, Philosophical Transactions of the Royal Society A: Mathematical, Physical and Engineering Sciences, 376, https://doi.org/10.1098/rsta.2017.0416, 2018.

Li, M., McNamara, A. K., and Garnero, E. J.: Chemical complexity of hotspots caused by cycling oceanic crust through mantle reservoirs,
795    Nature Geoscience, 7, 366–370, https://doi.org/https://doi.org/10.1038/ngeo2120, 2014a.

Li, X.-D. and Romanowicz, B.: Global mantle shear velocity model developed using nonlinear asymptotic coupling theory, Journal of Geophysical Research: Solid Earth, 101, 22 245–22 272, https://doi.org/10.1029/96jb01306, 1996.

Li, Y., Deschamps, F., and Tackley, P. J.: The stability and structure of primordial reservoirs in the lower mantle: Insights from models of thermochemical convection in three-dimensional spherical geometry, Geophysical Journal International, 199, 914–930,
800    https://doi.org/10.1093/gji/ggu295, 2014b.

Liu, J., Touboul, M., Ishikawa, A., Walker, R. J., and Graham Pearson, D.: Widespread tungsten isotope anomalies and W mobility in crustal and mantle rocks of the Eoarchean Saglek Block, northern Labrador, Canada: Implications for early Earth processes and W recycling, Earth and Planetary Science Letters, 448, 13–23, https://doi.org/10.1016/j.epsl.2016.05.001, 2016.

Lourenço, D. L., Rozel, A. B., and Tackley, P. J.: Melting-induced crustal production helps plate tectonics on Earth-like planets, Earth and
805    Planetary Science Letters, 439, 18–28, https://doi.org/10.1016/j.epsl.2016.01.024, 2016.

Lourenço, D. L., Rozel, A. B., Ballmer, M. D., and Tackley, P. J.: Plutonic-Squishy Lid: A New Global Tectonic Regime Generated by Intrusive Magmatism on Earth-Like Planets, Geochemistry, Geophysics, Geosystems, 21, https://doi.org/10.1029/2019GC008756, 2020.

Manga, M.: Mixing of heterogeneities in the mantle: Effect of viscosity differences, https://doi.org/10.1029/96GL00242, 1996.

Mashino, I., Murakami, M., Miyajima, N., and Petitgirard, S.: Experimental evidence for silica-enriched Earth's lower
810    mantle with ferrous iron dominant bridgmanite, Proceedings of the National Academy of Sciences, 117, 201917 096, https://doi.org/10.1073/pnas.1917096117, 2020.

Mckenzie, D. P., Roberts, J. M., and Weiss, N. O.: Convection in the earth's mantle: Towards a numerical simulation, Journal of Fluid Mechanics, 62, 465–538, https://doi.org/10.1017/S0022112074000784, 1974.

McNamara, A. K. and Zhong, S.: Thermochemical structures beneath Africa and the Pacific Ocean, Nature, 437, 1136–1139,
815    https://doi.org/10.1038/nature04066, 2005.

Merveilleux du Vignaux, N. and Fleitout, L.: Stretching and mixing of viscous blobs in Earth's mantle, Journal of Geophysical Research: Solid Earth, 106, 30 893–30 908, https://doi.org/10.1029/2001jb000304, 2001.

Morgan, J. P. and Morgan, W. J.: Two-stage melting and the geochemical evolution of the mantle: A recipe for mantle plum-pudding, Earth and Planetary Science Letters, 170, 215–239, https://doi.org/10.1016/S0012-821X(99)00114-4, 1999.

820    Mukhopadhyay, S.: Early differentiation and volatile accretion recorded in deep-mantle neon and xenon, Nature, 486, 101–104, https://doi.org/10.1038/nature11141, http://dx.doi.org/10.1038/nature11141, 2012.

Mulyukova, E., Steinberger, B., Dabrowski, M., and Sobolev, S. V.: Survival of LLSVPs for billions of years in a vigorously convecting mantle: Replenishment and destruction of chemical anomaly, Journal of Geophysical Research: Solid Earth, 120, 3824–3847, https://doi.org/10.1002/2014JB011688, 2015.

825    Murakami, M., Ohishi, Y., Hirao, N., and Hirose, K.: A perovskitic lower mantle inferred from high-pressure, high-temperature sound velocity data, Nature, 485, 90–94, https://doi.org/10.1038/nature11004, 2012.

Nakagawa, T. and Buffett, B. A.: Mass transport mechanism between the upper and lower mantle in numerical simulations of thermochemical mantle convection with multicomponent phase changes, Earth and Planetary Science Letters, 230, 11–27, https://doi.org/10.1016/j.epsl.2004.11.005, 2005.

830    Nakagawa, T. and Tackley, P. J.: Influence of magmatism on mantle cooling, surface heat flow and Urey ratio, Earth and Planetary Science Letters, 329-330, 1–10, https://doi.org/10.1016/j.epsl.2012.02.011, 2012.

Nakagawa, T. and Tackley, P. J.: Influence of combined primordial layering and recycled MORB on the coupled thermal evolution of Earth's mantle and core, Geochemistry, Geophysics, Geosystems, pp. 148–164, https://doi.org/10.4088/JCP.11m07343, 2014.

Nakagawa, T., Tackley, P. J., Deschamps, F., and Connolly, J. A.: The influence of MORB and harzburgite composition on thermo-chemical
835    mantle convection in a 3-D spherical shell with self-consistently calculated mineral physics, Earth and Planetary Science Letters, 296, 403–412, https://doi.org/10.1016/j.epsl.2010.05.026, 2010.

O'Neill, C., Lenardic, A., Weller, M., Moresi, L., Quenette, S., and Zhang, S.: A window for plate tectonics in terrestrial planet evolution?, Physics of the Earth and Planetary Interiors, 255, 80–92, https://doi.org/10.1016/j.pepi.2016.04.002, 2016.

O'Neill, C. J. and Zhang, S.: Lateral Mixing Processes in the Hadean, Journal of Geophysical Research: Solid Earth, 123, 7074–7089,
840    https://doi.org/10.1029/2018JB015698, 2018.

Pertermann, M. and Hirschmann, M. M.: Partial melting experiments on a MORB-like pyroxenite between 2 and 3 GPa: Constraints on the presence of pyroxenite in basalt source regions from solidus location and melting rate, Journal of Geophysical Research: Solid Earth, 108, 1–17, https://doi.org/10.1029/2000JB000118, 2003.

Peters, B. J., Carlson, R. W., Day, J. M., and Horan, M. F.: Hadean silicate differentiation preserved by anomalous 142Nd/144Nd ratios in
845    the Réunion hotspot source, Nature, 555, 89–93, https://doi.org/10.1038/nature25754, 2018.

Ritsema, J., Van Heijst, H. J., and Woodhouse, J. H.: Complex shear wave velocity structure imaged beneath Africa and Iceland, Science, 286, 1925–1931, https://doi.org/10.1126/science.286.5446.1925, 1999.

Rizo, H., Walker, R. J., Carlson, R. W., Horan, M. F., Mukhopadhyay, S., Manthos, V., Francis, D., and Jackson, M. G.: Geochem-
istry: Preservation of Earth-forming events in the tungsten isotopic composition of modern flood basalts, Science, 352, 809–812,
850    https://doi.org/10.1126/science.aad8563, 2016.

Rizo, H., Andrault, D., Bennett, N. R., Humayun, M., Brandon, A., Vlastelic, I., Moine, B., Poirier, A., Bouhifd, M. A., and Mur-
phy, D. T.: 182W evidence for core-mantle interaction in the source of mantle plumes, Geochemical Perspectives Letters, 11, 6–11,
https://doi.org/10.7185/geochemlet.1917, 2019.

Rozel, A. B., Golabek, G. J., Jain, C., Tackley, P. J., and Gerya, T. V.: Continental crust formation on early Earth controlled by intrusive
855    magmatism, Nature, 545, 332–335, https://doi.org/10.1038/nature22042, 2017.

Schierjott, J., Rozel, A., and Tackley, P. J.: On the self-regulating effect of grain size evolution in mantle convection models: Application to
thermochemical piles, Solid Earth, 11, 959–982, https://doi.org/10.5194/se-11-959-2020, 2020.

Shephard, G., Houser, C., Hernlund, J. W., Valencia-Cardona, J., Trønnes, R. G., and Wentzkovitch, R.: Seismological Expression of the Iron
Spin Crossover in Ferropericlase in the Earth's Lower Mantle, https://doi.org/10.31223/osf.io/deuck, 2020.

860    Sobouti, F., Ghods, A., and Arkani-Hamed, J.: On the advection of sharp material interfaces in geodynamic problems: Entrainment of the D"
layer, Journal of Geodynamics, 31, 459–479, https://doi.org/10.1016/S0264-3707(01)00012-6, 2001.

Solomatov, V. S. and Stevenson, D. J.: Suspension in convective layers and style of differentiation of a terrestrial magma ocean, Journal of
Geophysical Research, 98, 5375–5390, https://doi.org/10.1029/92JE02948, 1993.

Stein,    M.    and    Hofmann,    A.    W.:    Episodic    Crustal    Growth    and    Mantle    Evolution,    Nature,    372,    63–68,
865    https://doi.org/10.1180/minmag.1994.58a.1.219, 1994.

Stracke, A.: Earth's heterogeneous mantle: A product of convection-driven interaction between crust and mantle, Chemical Geology, 330-
331, 274–299, https://doi.org/10.1016/j.chemgeo.2012.08.007, 2012.

Tackley, P. J.: Self-consistent generation of tectonic plates in time-dependent, three-dimensional mantle convection simulations 2. strain
weakening and asthenosphere, Geochemistry, Geophysics, Geosystems, 1, https://doi.org/10.1029/2000gc000036, 2000.

870    Tackley, P. J.: Modelling compressible mantle convection with large viscosity contrasts in a three-dimensional spherical shell using the
yin-yang grid, Physics of the Earth and Planetary Interiors, 171, 7–18, https://doi.org/10.1016/j.pepi.2008.08.005, 2008.

Tackley, P. J.: Living dead slabs in 3-D: The dynamics of compositionally-stratified slabs entering a " slab graveyard" above the core-mantle
boundary, Physics of the Earth and Planetary Interiors, 188, 150–162, https://doi.org/10.1016/j.pepi.2011.04.013, http://dx.doi.org/10.
1016/j.pepi.2011.04.013, 2011.

875    Tackley, P. J.: Dynamics and evolution of the deep mantle resulting from thermal, chemical, phase and melting effects, Earth-Science Re-
views, 110, 1–25, https://doi.org/10.1016/j.earscirev.2011.10.001, 2012.

Tackley, P. J. and King, S. D.: Testing the tracer ratio method for modeling active compositional fields in mantle convection simulations,
Geochemistry, Geophysics, Geosystems, 4, 47 907, https://doi.org/10.1029/2001GC000214, 2003.

Tackley, P. J., Ammann, M. W., Brodholt, J. P., Dobson, D. P., and Valencia, D.: Mantle dynamics in super-Earths: Post-perovskite rheology
880    and self-regulation of viscosity, Icarus, 225, 50–61, https://doi.org/10.1016/j.icarus.2013.03.013, 2013.

Tange, Y., Kuwayama, Y., Irifune, T., Funakoshi, K. I., and Ohishi, Y.: P-V-T equation of state of MgSiO3 perovskite based on the MgO
pressure scale: A comprehensive reference for mineralogy of the lower mantle, Journal of Geophysical Research: Solid Earth, 117, 1–12,
https://doi.org/10.1029/2011JB008988, 2012.

Torsvik, T. H., Burke, K., Steinberger, B., Webb, S. J., and Ashwal, L. D.: Diamonds sampled by plumes from the core-mantle boundary,
885    Nature, 466, 352–355, https://doi.org/10.1038/nature09216, http://dx.doi.org/10.1038/nature09216, 2010.

45

Torsvik, T. H., Van Der Voo, R., Doubrovine, P. V., Burke, K., Steinberger, B., Ashwal, L. D., Trønnes, R. G., Webb, S. J., and Bull, A. L.: Deep mantle structure as a reference frame for movements in and on the Earth, Proceedings of the National Academy of Sciences of the United States of America, 111, 8735–8740, https://doi.org/10.1073/pnas.1318135111, 2014.

Touboul, M., Puchtel, I. S., and Walker, R. J.: 182W Evidence for Long-Term Preservation of Early Mantle Differentiation Products, Scienc, 890    335, 1065–1070, 2012.

Trampert, J., Deschamps, F., Resovsky, J., and Yuen, D.: Probabilistic tomography maps chemical heterogeneities throughout the lower mantle, Science, 306, 853–856, https://doi.org/10.1126/science.1101996, 2004.

Trønnes, R. G., Baron, M., Eigenmann, K., Guren, M., Heyn, B., Løken, A., and Mohn, C.: Core formation, mantle differentiation and core-mantle interaction within Earth and the terrestrial planets, Tectonophysics, 760, 165–198, 895    https://doi.org/https://doi.org/10.1016/j.tecto.2018.10.021, 2019.

Tsuchiya, T., Tsuchiya, J., Dekura, H., and Ritterbex, S.: Ab Initio Study on the Lower Mantle Minerals, Annual Review of Earth and Planetary Sciences, 48, 99–119, https://doi.org/10.1146/annurev-earth-071719-055139, 2020.

van der Hilst, R. D., Widiyantoro, S., and Engdahl, E. R.: Evidence for deep mantle circulation from global tomography, Nature, 386, 578–584, https://doi.org/10.1038/386578a0, 1997.

900    van Hunen, J., Zhong, S., Shapiro, N. M., and Ritzwoller, M. H.: New evidence for dislocation creep from 3-D geodynamic modeling of the Pacific upper mantle structure, Earth and Planetary Science Letters, 238, 146–155, https://doi.org/10.1016/j.epsl.2005.07.006, 2005.

van Keken, P. E. and Ballentine, C. J.: Whole-mantle versus layered mantle convection and the role of a high-viscosity lower mantle in terrestrial volatile evolution, Earth and Planetary Science Letters, 156, 19–32, https://doi.org/10.1016/s0012-821x(98)00023-5, 1998.

van Keken, P. E., King, S. D., Schmeling, H., Christensen, U. R., Neumeister, D., and Doin, M.-P.: A comparison of methods for the modeling 905    of thermochemical convection, Journal of Geophysical Research: Solid Earth, 102, 22 477–22 495, https://doi.org/10.1029/97jb01353, 1997.

Wang, W., Xu, Y., Sun, D., Ni, S., Wentzcovitch, R., and Wu, Z.: Velocity and density characteristics of subducted oceanic crust and the origin of lower-mantle heterogeneities, Nature Communications, 11, 1–8, https://doi.org/10.1038/s41467-019-13720-2, http://dx.doi.org/10.1038/s41467-019-13720-2, 2020.

910    Wang, W., Liu, J., Zhu, F., Wu, Z., and Dorfman, S. M.: Formation of large low shear velocity provinces through the decomposition of oxidized mantle, Nature Communications, 12, https://doi.org/10.1038/s41467-021-22185-1, http://dx.doi.org/10.1038/s41467-021-22185-1, 2021.

Waszek, L., Schmerr, N. C., and Ballmer, M. D.: Global observations of reflectors in the mid-mantle with implications for mantle structure and dynamics, Nature Communications, 9, 1–13, https://doi.org/10.1038/s41467-017-02709-4, 2018.

915    Wentzcovitch, R. M., Karki, B. B., Cococcioni, M., and de Gironcoli, S.: Thermoelastic Properties of MgSiO3-Perovskite: Insights on the Nature of the Earth's Lower Mantle, Physical Review Letters, 92, 4, https://doi.org/10.1103/PhysRevLett.92.018501, 2004.

Wolf, A. S., Jackson, J. M., Dera, P., and Prakapenka, V. B.: The thermal equation of state of ( Mg , Fe ) SiO 3 bridgmanite ( perovskite ) and implications for lower mantle structures, Journal of Geophysical Research B: Solid Earth, 120, 7460–7489, https://doi.org/10.1002/2015JB012108.Received, 2015.

920    Woodhead, J.: Mixing it up in the mantle, Nature, 517, 275–276, 2015.

Xie, L., Yoneda, A., Yamazaki, D., Manthilake, G., Higo, Y., Tange, Y., Guignot, N., King, A., Scheel, M., and Andrault, D.: Formation of bridgmanite-enriched layer at the top lower-mantle during magma ocean solidification, Nature Communications, 11, 1–10, https://doi.org/10.1038/s41467-019-14071-8, 2020.

Xu, W., Lithgow-Bertelloni, C., Stixrude, L., and Ritsema, J.: The effect of bulk composition and temperature on mantle seismic structure, Earth and Planetary Science Letters, 275, 70–79, https://doi.org/10.1016/j.epsl.2008.08.012, 2008.

Yamazaki, D. and Karato, S. I.: Some mineral physics constraints on the rheology and geothermal structure of Earth's lower mantle, American Mineralogist, 86, 385–391, https://doi.org/10.2138/am-2001-0401, 2001.

Yan, J., Ballmer, M. D., and Tackley, P. J.: The evolution and distribution of recycled oceanic crust in the Earth's mantle: Insight from geodynamic models, Earth and Planetary Science Letters, 537, https://doi.org/10.1016/j.epsl.2020.116171, 2020.

Yang, T. and Gurnis, M.: Dynamic topography, gravity and the role of lateral viscosity variations from inversion of global mantle flow, Geophysical Journal International, 207, 1186–1202, https://doi.org/10.1093/gji/ggw335, 2016.

Zhang, N., Zhong, S., Leng, W., and Li, Z. X.: A model for the evolution of the Earth's mantle structure since the Early Paleozoic, Journal of Geophysical Research: Solid Earth, 115, 1–22, https://doi.org/10.1029/2009JB006896, 2010.

Zhong, S. and Hager, B. H.: Entrainment of a dense layer by thermal plumes, Geophysical Journal International, 154, 666–676, https://doi.org/10.1046/j.1365-246X.2003.01988.x, 2003.

47